The Pennsylvania State University

The Graduate School

Department of Geosciences

LATE PLEISTOCENE SLIP RATES ALONG THE PANAMINT VALLEY FAULT ZONE, EASTERN CALIFORNIA

A Thesis in

Geosciences

by

William R. Hoffman

Submitted in Partial Fulfillment
of the Requirements
for the Degree of

Master of Science

December 2009

The thesis of William R. Hoffman was reviewed and approved* by the following:

Eric Kirby
Associate Professor of Geosciences
Thesis Advisor

Donald M. Fisher
Professor of Geosciences

Kevin Furlong
Professor of Geosciences

Peter C. LaFemina
Assistant Professor of Geosciences

Katherine H. Freeman
Professor of Geosciences
Associate Department Head of Graduate Programs

*Signatures are on file in the Graduate School

ABSTRACT

The Panamint Valley fault zone (PVFZ) is one of the primary structures accommodating right lateral shear across the Eastern California Shear Zone. Current slip-rate estimates are either long-term estimates based on total offset of the system and bounds on the initiation of fault slip, or estimates that rely on undated alluvial deposits. Using field surveys and high-resolution airborne LiDAR digital topography, I utilize displaced alluvial deposits at two localities, Happy Canyon and Manly Peak Canyon, to provide new slip-rate estimates along the PVFZ. Chronologic control is provided by a newly developed chronosequence of soils in Panamint Valley, radiocarbon dating of lacustrine tufa associated with shoreline deposits, and terrestrial cosmogenic nuclide (^{10}Be) dating of alluvial fan surfaces. At Manly Peak Canyon, debris flow levees offset 26.5 ± 3.8 m with a maximum surface age of 12.5 ± 1.4 ka yield a minimum extension rate of 2.1 ± 0.5 mm/yr. At Happy Canyon, displaced alluvial markers demonstrate that slip along northeast-striking fault strands in the right-stepping portion of the fault zone is purely dip-slip with no lateral component. Here, an alluvial fan complex cut by a series of normal faults with total extension of 56.0 ± 10.3 m has surface age estimates from a calibrated soil chronofunction ranging from ~16 - 40 ka, yielding a minimum extension rate of 2.7 ± 1.5 mm/yr. Additionally, a 20.7 ± 5.2 ka surface at Happy Canyon is cut by a fault scarp with 68.1 ± 2.0 m of vertical offset, which yields a preliminary Late Pleistocene minimum throw rate of 3.3 ± 0.7 mm/yr. Results from this thesis provide the only two slip-rate estimates along the PVFZ with chronologic control, and reveal along-strike variations in horizontal displacement direction that appear coordinated with increased subsidence in the northern part of the valley.

TABLE OF CONTENTS

LIST OF FIGURES

LIST OF TABLES

ACKNOWLEDGMENTS

First and foremost I would like to thank my advisor, Eric Kirby, for his mentorship and friendship throughout the duration of this project. I would also like to thank my committee members--Don Fisher, Kevin Furlong, and Pete LaFemina. They have provided many insightful and helpful suggestions that have improved this thesis. Colleagues in the tectonics lab and friends outside the lab have given me countless hours of help and support, for which I am extremely grateful. I want to acknowledge collaborators on this work who aided with parts of the methods, analysis, and interpretations. Physical and chemical separation of ^{10}Be was conducted at Kansas University with the assistance of Doug Walker and at the Purdue Rare Isotope Measurement Lab (PRIME) with the assistance of Darryl Granger. John Gosse from Dalhousie University provided advice on modeling of depth profiles and interpretation of ages. Eric McDonald from the Desert Research Institute in Reno, Nevada, led the description and analysis of soil development. All of these individuals, as well as my advisor, Eric Kirby, will be co-authors on the manuscripts that evolve from this thesis. The following people helped with the painstaking tasks of sample collecting, digging soil pits, and processing cosmogenic ^{10}Be samples: Willy Rittase, Christine Regalla, Steve Bacon, Sophie Baker, Graham Daldorf, Beate Mocek, Tom Clifton, and Penn State's 2008 Tectonic Geomorphology Class. Funding for this project has been provided by NSF, White Mountain Research Station Graduate Research Grant, GSA Graduate Research Grant, EarthScope, and the Shell Oil Graduate Fund.

Finally, I would like to thank my family for their continual encouragement, support, and guidance. I am greatly appreciative of everything they have done for me.

1 Introduction

Slip rates on active faults can provide insight into understanding the dynamics of rapidly deforming lithosphere. In particular, the temporal and spatial patterns of slip along active fault systems provide key constraints on fault system evolution, the distribution of strain across diffusely deforming regions, and the complex behavior of lithospheric deformation at plate boundaries. In eastern California, a broad zone of dextral shear occurs well inboard of the plate boundary, extending from the southern Mojave Desert (Dokka and Travis, 1990) to the Walker Lane in western Nevada. Geodetic studies indicate that shear across this zone, herein referred to as the Eastern California Shear Zone (ECSZ), accommodates 20-25% (9-12 mm/yr) of the relative motion (~48 mm/yr) between the Pacific plate and the stable interior of North America (e.g., Sauber et al., 1984; Dixon et al., 2000; Miller et al., 2001; Gan et al., 2003; Bennett et al., 2003). Geologic studies suggest that dextral shear is accommodated by slip on a distributed network of relatively young faults; estimates for the onset of dextral shear range from the Late Miocene (Dokka and Travis, 1990a, 1990b) to Pliocene (Monestaro et al., 2002; Faulds et al., 2005).

One of the outstanding questions in this region stems from the observation that slip rates inferred from displaced geologic markers can account for only ~50% of the present-day geodetic shear rate (e.g., Dokka and Travis, 1990b). Despite intensive efforts from researchers to quantify slip rates over Late Pleistocene timescales, this discrepancy between geologically and geodetically determined slip rates appears to persist. This suggests that it does not simply reflect an artifact of geologic rates that average many millions of years of deformation (e.g., Kirby et al., 2006, 2008; Oskin et al., 2007, 2008;

Frankel et al., 2007a, 2007b). It remains uncertain whether this discrepancy reflects 1) post-seismic transient deformation in the lower crust following recent earthquakes (e.g., Dixon et al., 2003; Oskin et al., 2008), 2) time periods of alternating fault activity and quiescence (Peltzer et al., 2001; Dolan et al., 2007), or 3) significant, off-fault deformation as yet unaccounted for in geologic slip budgets.

Recent studies of fault systems in the Death Valley – Sierra Nevada region reveal additional complexity in the spatial pattern of fault slip rate. Although slip rate is often assumed to be conserved along strike of an individual fault zone, such that a single rate determination is sufficient to characterize the entire fault length, studies of the growth of fault systems internal to deforming regions indicate that displacement is expected to vary along the length of a fault (e.g., Cowie and Scholz, 1992). Recent determinations of Late Pleistocene – Holocene slip rate along the Death Valley – Furnace Creek – Fish Lake Valley fault system (e.g., Reheis and Sawyer, 1997; Frankel et al., 2007a, 2007b) and along the Owens Valley – White Mountain fault zone (Lee et al., 2001; Bacon and Pezzopane, 2007; Kirby et al., 2006, 2008) reveal significant spatial variations in fault slip rate along strike (Figure 1-1). Specifically, slip appears to die out along these faults as they approach the Garlock fault, a 260-km-long northeast- to east-striking left-lateral fault (Figure 1-1). These slip-rate gradients suggest significant spatial variability in how strain is accommodated along the ECSZ, or that fault systems are still lengthening. Thus, although the geologic budget of deformation rate across the ECSZ nearly matches geodetically-determined velocities along a transect across the central portions of the Death Valley, Hunter Mountain, and Owens Valley faults (e.g., Frankel et al., 2007a; Lee et al., 2009), significant mismatches still remain at the northern

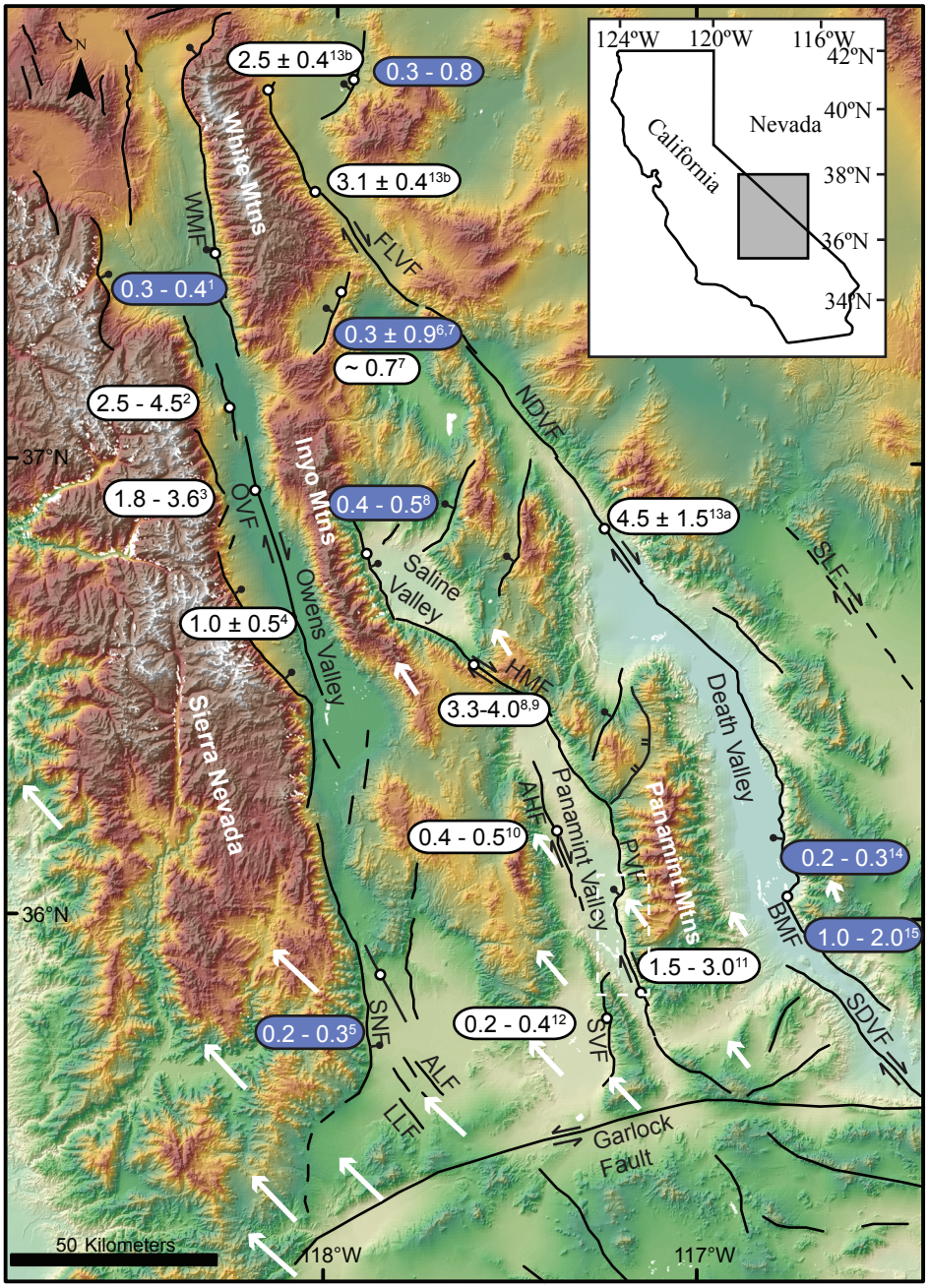

Figure 1-1: Map of the eastern California shear zone (ECSZ) with Holocene - Late Pleistocene geologic slip rates (mm/yr) (white circles). Study area for this thesis outlined in white box. Blue bubbles represent normal or oblique-normal geologic slip rates, white bubbles represent right-lateral geologic slip rates. Geodetic rates across latitudes 37-37.5°N: 9.3 ± 0.2 mm/yr (Bennett et al., 2003); 36.5°N: 11-13 mm/yr (Gan et al., 2000); and 36°N: 11-13 mm/yr (this study, based on PBO stations). Arrows represent velocity vectors from PBO arrays. Major fault zones of the ECSZ: AHF-Ash Hill fault; ALF-Airport Lake fault; BMF-Black Mountain fault; FLVF-Fish Lake Valley fault; HMF-Hunter Mountain fault; LLF-Little Lake fault; NDVF-Northern Death Valley fault; OVF-Owens Valley fault; PVF-Panamint Valley fault; SDVF-Southern Death Valley fault; SLF-State Line fault; SNF-Sierra Nevada frontal fault; SVF-Searles Valley fault; WMF-White Mountain fault. References for slip rates: [1] Kirby et al., 2006; [2] Kirby et al., 2008; [3] Lee et al., 2001; [4] Bacon and Pezzopane, 2007; [5] Le et al., 2007; [6] Reheis and Sawyer, 1997; [7] Lee et al., 2001; [8] Lee et al., 2009; [9] Oswald and Wesnousky, 2002; [10] Densmore and Anderson, 1997; [11] Zhang et al., 1990; [12] Numelin et al., 2007; [13] Frankel et al., 2007a, 2007b; [14] Knott et al., 2001; [15] Klinger et al., 1999.

and southern ends of these fault systems. Notably, both the southern Owens Valley fault system (Airport Lake and Little Lake faults) and the Black Mountain fault in southern Death Valley appear to have low slip rates (<1-2 mm/yr, Klinger, 1999; Roquemore, 1988). The Panamint Valley fault zone (PVFZ), which lies between southern Owens and Death Valleys, represents a major gap in the slip-rate catalogue; current estimates either rely on undated alluvial deposits (Zhang et al., 1990; Oswald and Wesnousky, 2002) or represent long-term estimates based on total offset of the system and bounds on the initiation of fault slip (Burchfiel et al., 1987; Lee et al., 2009).

In this thesis, I seek to test the hypothesis that slip along the Panamint Valley fault zone accommodates the majority of shear across the ECSZ directly north of the Garlock fault. I address this problem by developing new estimates of slip rate along the Panamint Valley fault zone over Late Pleistocene timescales. I utilize displaced alluvial fan deposits at two localities along the southern portion of the fault system and reconstruct fault slip from field surveys using differential GPS (dGPS) and airborne LiDAR digital topographic data. Chronologic control is provided by radiocarbon dating of tufa associated with lacustrine shorelines, soil characteristics, and terrestrial cosmogenic nuclide (^{10}Be) dating of alluvial fan surfaces. Results from this thesis provide new constraints with which to assess spatial variations of slip along major fault systems as they approach the Garlock fault, thus contributing to a better understanding of the rates and patterns of strain release across this portion of the ECSZ.

This thesis is organized into one chapter incorporating 1) a detailed evaluation of the slip rate along the southern Panamint Valley fault zone where it crosses the alluvial fan complex at the head of Manly Peak Canyon, revisiting a site used by Zhang et al.

(1990) to estimate Holocene slip rate along the southern Panamint Valley fault zone; and 2) a preliminary evaluation of the slip rate along the central Panamint Valley fault zone at the mouth of Happy Canyon, located ~20 km north of Manly Peak Canyon.

For both sites, slip rates are constrained by maps of alluvial deposits, surveys of displaced geomorphic markers, characterization of soil development, and chronologic data; including radiocarbon ^{14}C dating of low elevation lacustrine shorelines preserved along the eastern flank of southern Panamint Valley. The low elevation shoreline data provide a key chronologic marker in the landscape, as cross-cutting relationships with alluvial deposits provide direct constraints on relative age of alluvial deposits and the degree of soil development. These data, combined with a radiocarbon ^{14}C age from a log embedded in a faulted debris flow and a ^{10}Be depth profile, provide key calibration points for developing a soil chronofunction, an empirical relationship of how soil characteristics vary with age.

At Manly Peak Canyon, the soil chronofunction is then used in conjunction with direct surface dating using ^{10}Be exposure ages from boulders and cross-cutting relationships with dated low-elevation shoreline features to determine the age of displaced debris flow levees. At Happy Canyon, age estimates for displaced alluvial fans are provided by the soil chronofunction. However, samples from two ^{10}Be depth profiles and two ^{36}Cl depth profiles are currently awaiting AMS analysis at PRIME Lab (Purdue), and will eventually provide direct age control of alluvial fans at Happy Canyon offset by the Panamint Valley fault zone. Therefore, I consider the slip-rate estimates reported at Happy Canyon to be preliminary rates.

By determining Late Pleistocene slip rates at multiple locations, I test whether differences in geometry and character along-strike of the PVFZ are associated with along-strike variations in slip-rate over Pleistocene timescales. These data provide the first slip rates with chronologic control along the PVFZ, and provide an opportunity to assess spatial variations of slip rate and displacement direction along strike of this major fault system. Finally, I incorporate the new slip rates into the geologic slip-rate budget of faults north of the Garlock fault to assess if these new rates can reconcile the ~5 mm/yr difference between geologic and geodetic rates of deformation across the Eastern California Shear Zone at ~36°N.

2 Late Pleistocene Slip Rates along the Panamint Valley Fault Zone

2.1 Active Tectonics of the Eastern California Shear Zone

The ECSZ is a region of rapid dextral shear that extends from the eastern end of the Big Bend of the San Andreas fault into the region between the Sierra Nevada and the Basin and Range Province (Figure 1-1). Within the ECSZ, the Garlock fault—a 260-km-long northeast- to east-striking left-lateral fault—forms a physiographic boundary between the mountainous, high-elevation regions of the Sierra Nevada and Basin and Range to the north, and the lower, more subdued topography to the south. South of the Garlock fault, right-lateral shear across the ECSZ is accommodated along a series of parallel, mostly discontinuous, right-lateral strike-slip faults, except in the northeastern Mojave, where clockwise rotation of blocks bounded by east-striking left-lateral faults appears to accommodate active shear (e.g., Dokka and Travis, 1990; Schermer et al., 1996; Oskin et al., 2008). North of the Garlock fault, shear along the ECSZ is distributed among three transtensional fault zones: the Owens Valley—White Mountain, Panamint Valley - Hunter Mountain, and Death Valley—Fish Lake fault zones (Figure 1-1).

The interplay between transcurrent shear in the ECSZ along individual faults and the older, but still active, Garlock fault remains a mystery. The Garlock fault is one of the principal faults in eastern California, and began accommodating deformation in the Middle to Late Miocene; it has since accommodated 48-64 km of left-lateral displacement (e.g., Smith, 1962; Smith and Ketner, 1970; Davis and Burchfiel, 1973; McGill, 1991; Monastero et al., 1997). Curiously, nowhere does the Garlock fault appear to offset, or be offset by, NW-trending faults of the ECSZ (Frankel et al., 2008). It is

clear that individual strike-slip faults of the ECSZ to both the north and south do not pass through the Garlock fault, despite geodetic data that show the north to northwest-oriented strain field to be relatively continuous across the Garlock (e.g., Peltzer et al., 2001); velocities are orientated at a high angle to the Garlock fault, with little to no discernable shear parallel to the fault itself (e.g., Miller et al., 2001; McGill et al., 2009). How exactly strain is transferred across or around the Garlock fault, however, remains uncertain.

In efforts to understand the distribution of fault slip on major fault systems as they approach the Garlock fault, studies have focused on quantifying Late Pleistocene – Holocene patterns of deformation along faults within the ECSZ north of the Garlock fault. These studies collectively reveal significant spatial variations in fault slip rate, decreasing toward the ends of the fault zones. The Fish Lake Valley fault zone exhibits right-lateral slip rates of 2-3 mm/yr, whereas the central portion of the Death Valley fault zone is known to slip at rates of 4-5 mm/yr (Frankel et al., 2007b, 2007a). In contrast, the Black Mountain fault in the southern portion of the Death Valley fault zone exhibits slip rates of only ~ 1 mm/yr (Klinger, 1999). Similar variations in slip rate occur along the Owens Valley, where the northern (White Mountain fault zone) and southern (Owens Valley fault) fault segments appear to have slip rates between 0.5 and 1 mm/yr (Kirby et al., 2006; Bacon and Pezzopane, 2007), whereas the central Owens Valley fault zone appears to have slip rates between 3 – 4 mm/yr (Lee et al., 2001; Kirby et al., 2008) (Figure 1-1).

It has been suggested that the Panamint Valley – Hunter Mountain fault system plays a central role in accommodating displacement variations along the ECSZ. Reheis and Dixon (1996) suggested that slip along the Panamint Valley - Ash Hill fault zone is

transferred northward to the Death Valley fault system, across a series of northeast-striking normal faults in the Saline Valley – Tin Mountain region (Figure 1-1). This architecture, in conjunction with low slip rates in southern Death and Owens Valleys, suggests that the Panamint Valley fault zone may accommodate the majority of shear in eastern California north of the Garlock fault. However, few chronologic data are available to constrain slip rates along the Panamint Valley fault zone, and current estimates rely on either long-term averages determined over the past 4 Ma (e.g., Burchfiel et al., 1987) or assumed ages of geomorphic features (e.g., Zhang et al., 1990; Oswald and Wesnousky, 2002). Without refined chronologic constraints on displacements, it is not possible to fully assess the role the Panamint Valley fault zone plays in accommodating right lateral shear north of the Garlock fault. The main goal in this study, therefore, is to provide quantitative estimates of slip rate along the Panamint Valley fault zone over Late Pleistocene time.

2.2 Background: Geology of Panamint Valley

2.2.1 Plio-Quaternary Evolution of Panamint Valley

Panamint Valley is located in eastern California, bounded by the Panamint Range, which separates Panamint Valley from Death Valley to the east, and the Argus Range and Slate Range to the west, which separate Panamint Valley from the Owens and Searles Valleys to the west (Figure 2-1). Panamint Valley is an extensional basin bounded on the east by active oblique-slip normal faults associated with the Panamint Valley fault zone (Smith, 1976; Burchfiel et al., 1987; Zhang et al. 1990). This fault system is linked to the

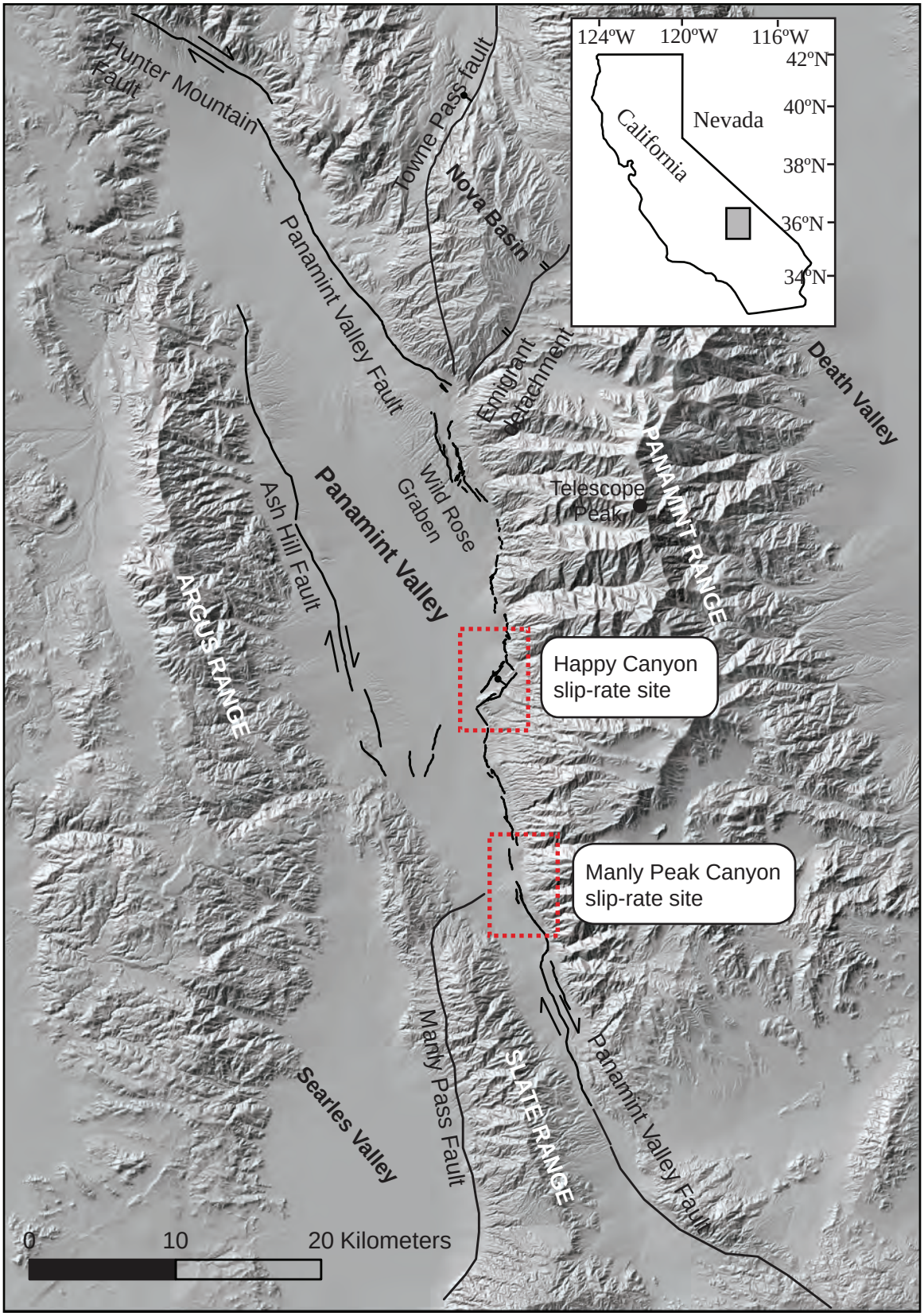

Figure 2-1: Overview of the geometry of Panamint Valley, with slip-rate sites used in this study outlined in red.

north with a northwest-striking, right-lateral strike-slip fault, the Hunter Mountain fault zone. Coordinated slip on both fault systems leads to basin subsidence, and as such, Panamint Valley is considered an archetypical example of a "pull-apart" basin (e.g., Burchfiel and Stewart, 1966). The valley itself is long and narrow, extending more than 100 km in length, with ~3,000 m of vertical relief between the valley floor (311 m) and the top of the Panamint Range, Telescope Peak, at 3368 m (Figure 2-1).

The fault system that bounds the eastern side of Panamint Valley exhibits a multi-stage evolution during late Cenozoic extension in the southwestern Basin and Range province. In the northern part of the Panamint Range, a series of low-angle normal faults, collectively termed the Emigrant detachment, separate greenschist-grade metamorphic rocks of the Panamint Range from Miocene—Pliocene sedimentary and volcanic deposits in the Nova Basin (e.g., Hodges et al., 1989; Snyder and Hodges, 2000) (Figure 2-1). The Emigrant detachment merges with the active range front fault in the vicinity of Wildrose Graben, and it appears that the southern range front fault may have reactivated this Miocene detachment (Andrew and Walker, 2009) (Figure 2-1). This is consistent with recent reconstructions of slip along the Panamint Valley fault system that suggest the southern fault accomplished ~17 km of displacement during the past 15 Ma (Andrew and Walker, 2009).

Initiation of the modern Panamint Valley fault zone is broadly constrained between 2.8 and 4 Ma. Basalts with identical chemistry and similar age (3.7 – 4 Ma, Burchfiel et al., 1987) are present on both sides of northern Panamint Valley. However, magnetic surveys show that the basalts are absent beneath the valley fill (MIT and Biehler, 1987), suggesting they pre-date opening of northern Panamint Valley. As such,

they provide a maximum age constraint on the development of the modern fault system. Moreover, because these same basalts cap a subvertical contact between the Jurassic Hunter Mountain batholith and its country rock, they form a piercing point that suggests a total displacement of ~9 km along the Hunter Mountain fault (Burchfiel et al., 1987). Thus, the northern part of the modern fault system appears to be younger than the southern portion, and to have developed in the past 4 Ma. This constraint only provides a maximum age, and it is possible that the modern fault system initiated more recently. Lee et al. (2009) proposed that rapid cooling observed in the footwall of the Saline Valley normal fault at ~2.8 Ma signaled the onset of Pliocene slip along this fault system, and suggested that this was a better estimate for the initiation of the Hunter Mountain fault.

Given the transfer fault interpretation for the Hunter Mountain fault zone (HMFZ) (e.g., Burchfiel et al., 1987), the displacement on the central segment of the structure is equal to the amount of extension in both northern Panamint Valley and Saline Valley (Burchfiel et al., 1987). Utilizing this interpretation, previous geologic slip-rate studies use the Hunter Mountain fault as a proxy to determine slip-rate constraints on the PVFZ. Based on the 9 km offset of a bedrock piercing point, the long-term slip rate along the PVFZ is at least 2 – 3 mm/yr if initiation occurred ~3.7 – 4.0 Ma (Burchfiel et al., 1987), and ~ 3.2 mm/yr if the initiation of this fault system was actually ca. 2.8 Ma (Lee et al., 2009).

2.2.2 Active Faulting in Panamint Valley

As noted above, the PVFZ is an oblique-slip normal fault that bounds the eastern side of Panamint Valley. Prominent scarps developed in Late Pleistocene to Holocene alluvial deposits are present along ~100 km of the range front, attesting to recent activity along nearly the entire length of the fault zone (e.g., Smith, 1976). The geometry of the active fault system has been the source of some debate. Low-angle normal faults are recognized within the range, in the vicinity of Happy, Pleasant, and South Park Canyons (Figure 2-2). These faults separate a package of Plio-Quaternary fanglomerates from brecciated bedrock within the range (Cichanski, 2000; Walker et al., 2005). Although early workers considered these range-front faults to have been abandoned during the Pleistocene, in favor of a high-angle, strike-slip fault (Smith, 1976; Zhang et al., 1990; Cichanski, 2000), more recent work has shown that the kinematics of slip along this fault system are consistent with a low-angle structure (Kirby et al., 2004; Walker et al., 2005; Andrew and Walker, 2009).

A secondary structure, the Ash Hill fault, extends along the western side of the valley for ~50 km; active strands extend from as far south as the Slate Range to the northern valley (Figure 2-1). The Ash Hill fault appears to be a steep (~80°W dip) fault that is likely a splay in the hanging wall of the Panamint Valley fault zone (Densmore and Anderson, 1997). Right-lateral displacement of a 4.05 ± 0.15 Ma basalt by 1.2 ± 0.3 km and a strike-slip to dip-slip ratio of 5:2:1 (slip vector oriented toward 320° - Densmore and Anderson, 1997) suggest a minimum long-term slip rate of the Ash Hill fault of 0.3 ± 0.1 mm/yr (Densmore and Anderson, 1997). Although it is possible that the

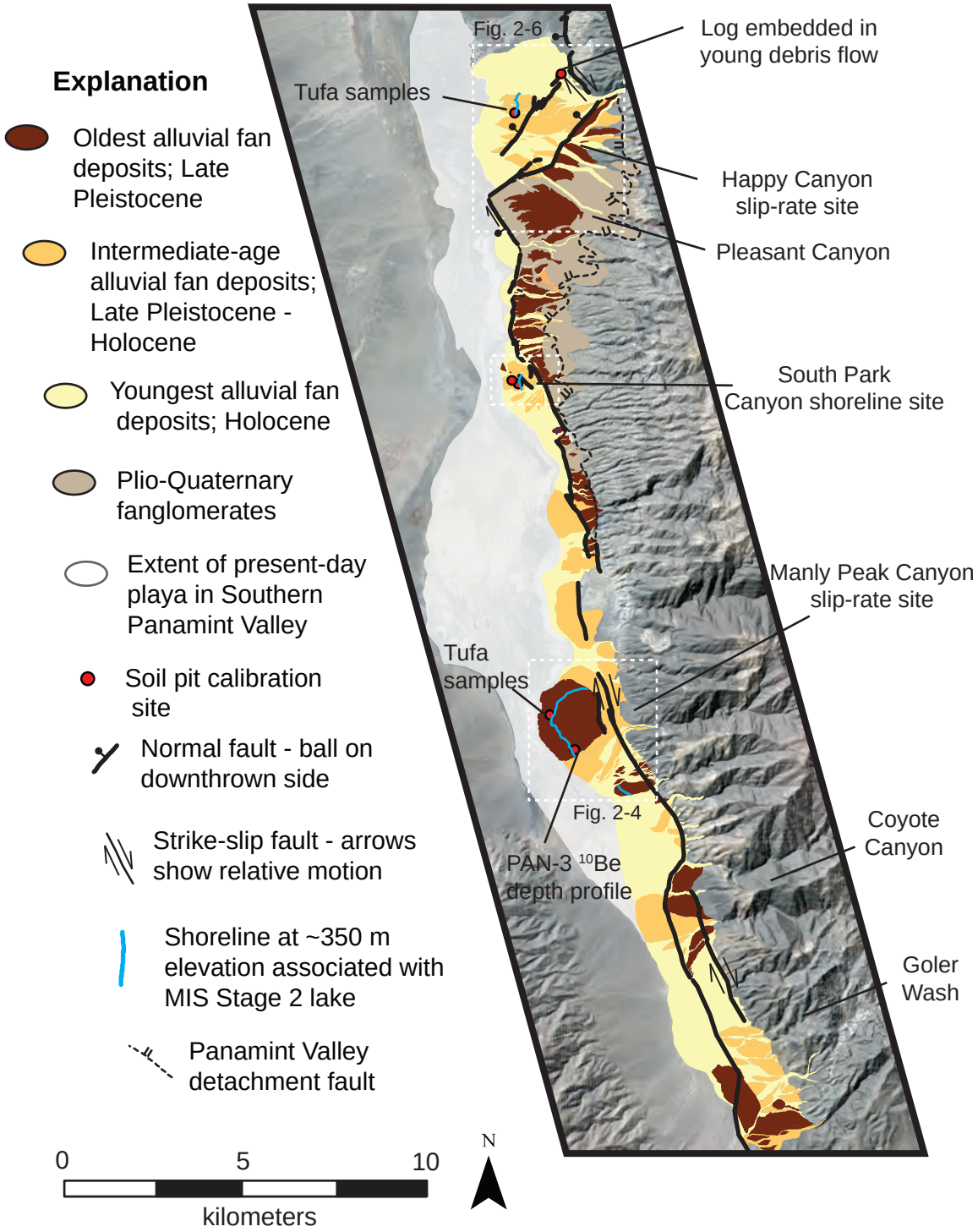

Figure 2-2: Geologic mapping of Quaternary alluvial fans on the central-southern portion of the Panamint Valley fault zone on the eastern side of Panamint Valley. Location of slip-rate studies at Happy Canyon and Manly Peak Canyon are outlined in dashed white lines.

Ash Hill fault also initiated more recently than ~4 Ma, constraints on the Late Pleistocene slip rate on this fault system are lacking at present.

Additionally, the PVFZ exhibits along-strike changes in geometry and character that suggest the possibility of along-strike variations in slip rate. In the south, Panamint Valley is narrow, and the primary trace of the PVFZ occurs in the center of the valley and exhibits primarily strike-slip motion (Smith, 1976). Near Goler Wash, however, prominent fault scarps indicate activity along the range-front normal fault, and at the Manly Peak Canyon site, the fault system appears to be partitioned between strike-slip and normal slip (Figure 2-2). North of this point, however, the fault system has a different character. The valley itself is wider, and a rhomb-shaped playa with a significant negative gravity anomaly (e.g., Walker et al., 2005) that attests to locally-significant subsidence. The northwestern margin of this rhomboid sub-basin is coincident with the Ash Hill fault, which is expressed as a series of distributed right lateral strike slip faults that displace Pleistocene alluvial fans (Figure 2-1). This section of the Panamint Valley fault is developed along the range front, coincident with a Plio-Quaternary low-angle normal fault system preserved in the footwall (Cichanski, 2000) (Figure 2-2). Finally, on the basis of changes in the relative size of alluvial fans, Walker et al. (2005) suggested that subsidence rates were greater north of the Manly Peak Canyon fan. All of these characteristics suggest the presence of significant along-strike variations in the rate and nature of deformation along the fault system.

2.2.3 Late Pleistocene Pluvial History of Southern Panamint Valley

At times during the Quaternary, Panamint Valley was part of a chain of lakes in eastern California and western Nevada that extended from the Sierra Nevada to Death Valley and fed from glacial melting in the Sierra Nevada (e.g., Smith, 1976). These pluvial lakes, a term given to lakes that have experienced large fluctuations in area and volume in response to climatic variations, were connected via the Owens River to a chain of lakes in the Indian Wells (China Lake) and Searles Valleys (Gale, 1914) (Figure 2-3). Searles Lake was connected at highstand levels across a 690 m sill (Smith and Street-Perot, 1983) to Panamint Valley, which in turn spilled through Wingate Wash (sill elevation of ~610 m) into Death Valley (Smith, 1976). During the Quaternary, Searles and Panamint Valleys have filled to overflowing on five or six occasions (Jannik et al., 1991), and the most recent highstand appears to have been between ~120-150 ka (Densmore and Anderson, 1997), during Marine Isotope Stage (MIS) 6. The age and duration of subsequent lacustrine occupation of Panamint Valley is the matter of some debate (e.g., Jayko et al., 2008). Low-elevation (320 - 350 m) shorelines are preserved within southern Panamint Valley (Smith, 1976) and have been presumed to represent a shallow (~20-30 m depth) lake during the latest Pleistocene (MIS 2). However, Jayko and others (2008) obtained radiocarbon ages from higher elevation lacustrine tufa (between elevations of 400 m and 510 m) suggestive of a MIS 2 age. Dating of the same deposits using the production of cosmogenic ^{36}Cl, however, yield much older ages consistent with MIS 4 occupation (Jayko et al., 2008), and thus, the duration and extent of latest Pleistocene (MIS 2) lakes in Panamint Valley remain uncertain.

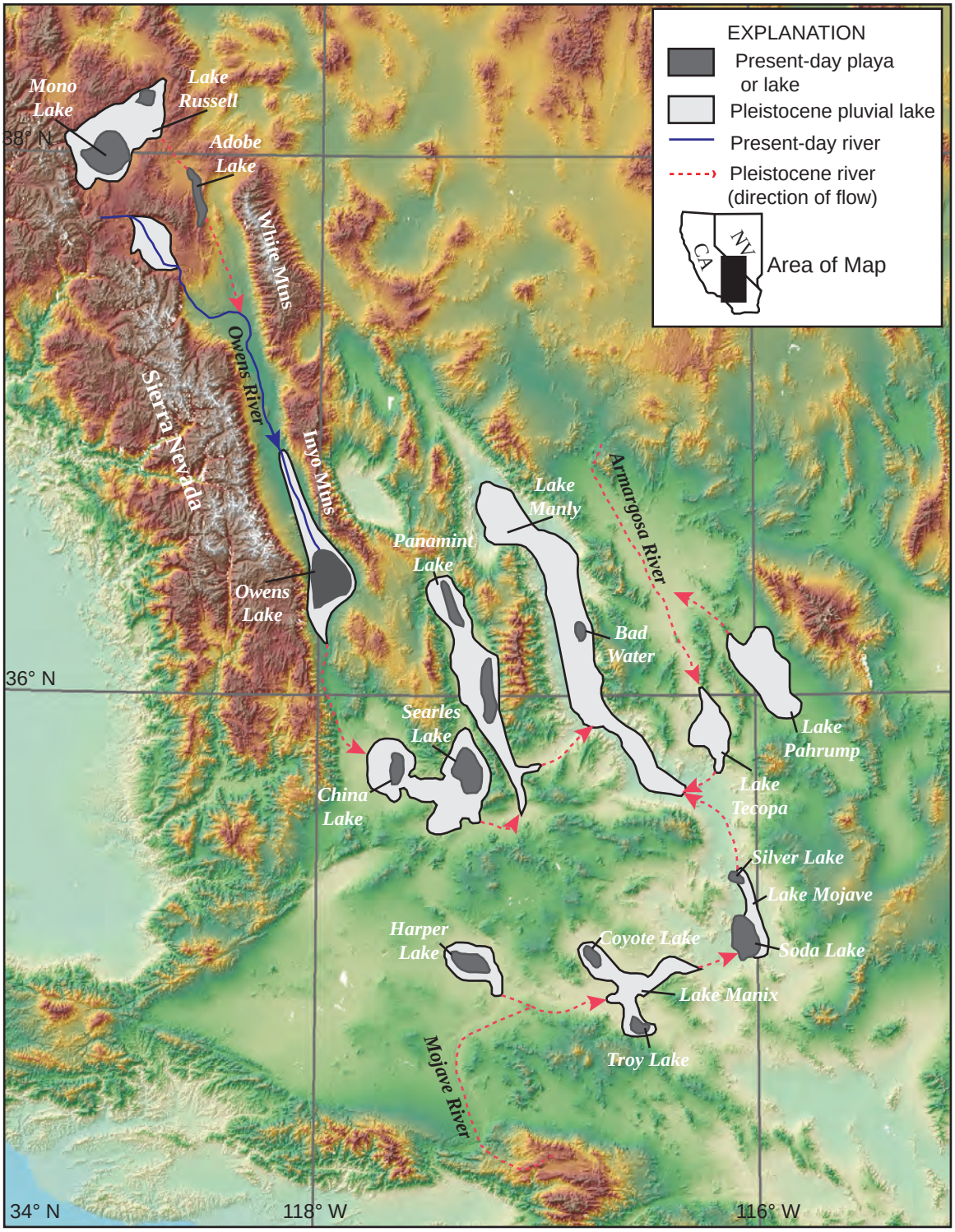

Figure 2-3: Map of present day and late Pleistocene Owens River system in the western US, with hydrologically connected chain of pluvial lakes fed by discharge from the Sierra Nevada Mountains (Figure modified from Jannik et al., 1991).

2.2.4 Previous Work on Pleistocene Slip Rates along the PVFZ

Oswald and Wesnousky (2002) noted displaced channels along the Hunter Mountain fault that they inferred to post-date 15 ka, and from these inferred a Late Pleistocene slip rate of ~3.3 - 4.0 mm/yr. Likewise, the only work along the southern Panamint Valley fault relied on an assumed chronology for Late Pleistocene alluvial deposits (Zhang et al., 1990). These authors utilized displaced debris-flow deposits near Manly Peak Canyon (Figure 2-2) and suggested a slip rate of ~2.4 ± 0.8 mm/yr for the southern PVFZ.

All of these studies are subject to significant uncertainty, however. Rates averaged over million-year timescales are subject to inferences regarding when fault slip began (c.f., Burchfiel et al., 1987; Lee et al., 2009) and may also mask important temporal variability in strain release at shorter timescale (e.g., Friedrich et al., 2003; Kirby et al., 2006). Studies that utilized displaced geomorphic features and alluvial deposits, and do not rely on a direct chronology, are likewise subject to uncertainties that stem from the assumed chronology.

In this thesis, I re-visit displaced geomorphic markers at Manly Peak Canyon, a site used by Zhang et al. (1990) to estimate a Holocene slip rate of ~1.1 - 2.4 mm/yr, and evaluate displaced alluvial fan surfaces at Happy Canyon, 20 km north of Manly Peak Canyon. Newly-acquired LiDAR topography (http://www.opentopography.org/) and high-precision topographic surveys provide new constraints on the magnitude of slip. I combine these with new chronology provided by 1) a locally-calibrated soil chronosequence and 2) direct dating of boulders present on the alluvial surface at Manly Peak Canyon to determine slip-rates along the central and southern Panamint Valley fault

zone during the Late Pleistocene. By evaluating slip rates at two sites, I test whether differences in geometry and character along-strike of the PVFZ are indeed associated with variations in slip rate over Pleistocene timescales.

2.3 Manly Peak Canyon Site

In an effort to characterize the relative age and distribution of faulting in Panamint Valley, I mapped Quaternary faults and alluvial deposits on the eastern side of Panamint Valley between Happy Canyon and Goler Wash (Figure 2-2), with particular emphasis focused on using alluvial surfaces as geomorphic markers of fault displacement. Alluvial fan complexes on the eastern side of Panamint Valley, sourced from the Panamint Range, preserve multiple generations of depositional lobes which exhibit distinguishing surface and soil characteristics (e.g., Wells et al., 1986) that form the basis for my mapping.

I distinguish three general classes of alluvial fans on the basis of surface morphology, the degree of desert pavement development, and soil characteristics. In ascending relative age (youngest to oldest), I refer to these as Q4, Q3, and Q2, respectively. In general, the youngest units (Q4) are characterized by distinct, relict depositional morphology (bar and swale), weak to light degree of varnish accumulation on clasts exposed at the surface, and thin (0-2 cm) Av horizons (Table 2.1). Fan surfaces of intermediate age (Q3) are distinguished by a greater degree of varnish development on clasts, thicker (3-5 cm) Av horizons, subdued depositional morphology, and moderate shattering of surface clasts. The oldest surfaces (Q2) lack any relict depositional

Table 1.1. MAPPING CRITERIA FOR ALLUVIAL FAN DEPOSITS IN SOUTHERN PANAMINT VALLEY

Unit Name	Surface Form	Desert Varnish	Soil Development
Q4	Youngest alluvium; occurs adjacent to and above modern washes; broadly Holocene in age	Weak on some surface boulders or a complete lack of altogether	Non-existent to thin AV horizon, 0-1 cm thick
Q4a	Fresh depositional morphology; little to no pavement development; bars preserve imbricate clasts	Incipient varnish on a few clasts	Negligible soil development; no AV horizon
Q4b	Well preserved depositional morphology; incipient pavement development in swales	Light redish-brown coating on clasts; incipient-weak degree of rubification	Weak soil development; thin AV horizon less than 5 mm
Q4c	Debris flow topography with channel levees; poorly developed pavement surrounds moderately developed areas; moderately developed pavement has unsorted, interlocking clasts	Thin-moderate continuous varnish on clasts; begin seeing occasional fractured clasts; weak-moderate degree of rubification	Moderate soil development; noticeable AV horizon up to 1cm thick
Q3	Intermediate age alluvium; occurs adjacent to and above Q4 surfaces; broadly late Pleistocene in age; minor debris flow and bar and swale morphology; unsorted, interlocking clasts in moderate to well developed pavement in some places	Continuous, moderate degree of varnish on surface clasts; dark brown to blue-black; moderate-strong degree of rubification	Moderate to strong soil development; AV horizon at least 1-5 cm thick in most soils
Q3y	Debris flow morphology with channel levees; weak pavement in channels; well-preserved, large boulders; minor bar and swale morphology in distal part of fan; unsorted, interlocking clasts in moderately well developed pavement on distal parts of the fan	Thin to moderately continuous dark-brown varnish on clasts; moderate degree of rubification on underside of clasts	Moderate soil development; AV horizon 1-5 cm thick
Q2	Oldest alluvium; occurs adjacent to and above Q3 and Q4 surfaces; broadly late Pleistocene in age; Dissected; little to no surface morphology preserved; well-packed interlocking clasts in continuous, well-developed pavement; shattered boulders	Strong, continuous varnish on clasts ranging from dark brown-black to shiny blue-black; strong degree of rubification on underside of clasts	Strong soil development; AV horizon 5-10 cm thick; soils dark brown-red

morphology, exhibit desert pavements with strong interlocking of clasts, are strongly varnished, and have thick (5 – 10 cm) Av horizons. Although I recognize that these surface characteristics may vary with parent material as well as age, they provide a first-order basis for mapping of alluvial deposits. In addition, the degree of soil development was characterized (e.g., Harden, 1982) by Eric McDonald beneath several key surfaces where independent age control was available (see section below).

South of Manly Peak Canyon, alluvial fan complexes at the foot of the Panamint Range are dissected by faults associated with the PVFZ (Figure 2-4). Multiple generations of fan surfaces are present at Manly Peak Canyon, and fault scarps cut all surfaces except the active wash (Zhang et al., 1990). The PVFZ at this location consists of a series of north-northwest striking faults near the head of the fan; scarps along these faults exhibit evidence for both strike-slip displacement and normal slip (Figure 2-4). First recognized by Smith (1976), two prominent debris-flow levees define the margins of an 8-10 m wide channel that is displaced in a right-lateral sense across the primary strand of the PVFZ (Figure 2-5). Previous surveying at this site (Smith, 1976; Zhang et al., 1990) focused on the dextrally-offset levees, and determined 17 – 27 m of dextral slip. Here, I re-evaluate these displacement estimates using two data sources: 1) a high-resolution topographic map of the site generated from a detailed survey using differential GPS, and 2) recently-acquired airborne LiDAR (Light Detection And Ranging) data. Both data sets provide sub-meter precision of surface topography to calculate displacement magnitude. In addition, both studies fail to account for slip on a range-bounding normal fault that displaces the same channel system. Here, I consider both fault segments in the reconstruction of total fault slip (c.f., Walker et al., 2005).

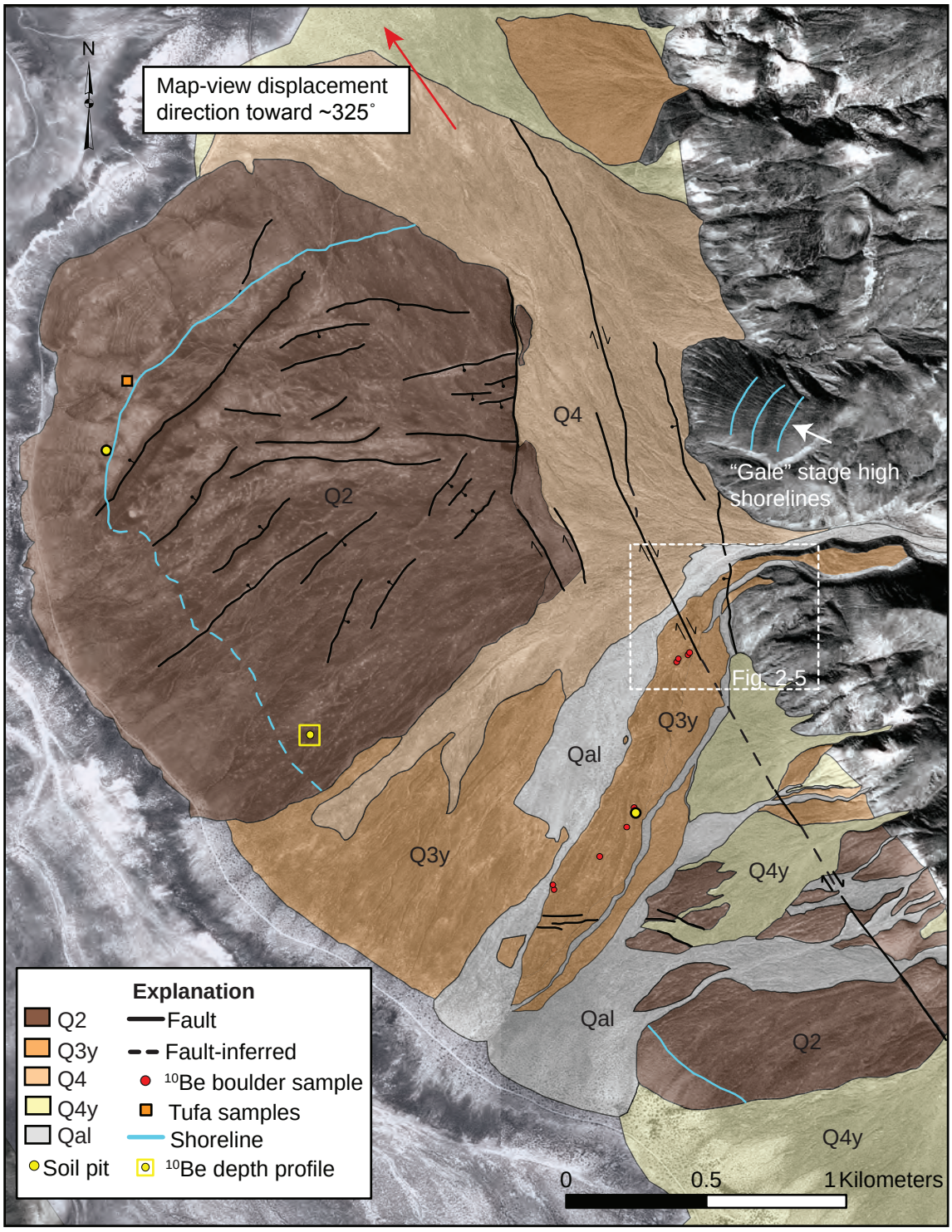

Figure 2-4: Digital Orthophoto of Manly Peak Canyon slip-rate site with mapped faults and Quaternary alluvial fans. White box outlines the Q3y surface offset by a normal and right lateral strand of the PVFZ. Low-elevation shorelines are visible on the Q2 surface to the north and south of the Q3y debris flow surface at ~350 m elevation. Note there are no shorelines present on the Q3y debris flow surface, even though the fan surface extends below 350 m.

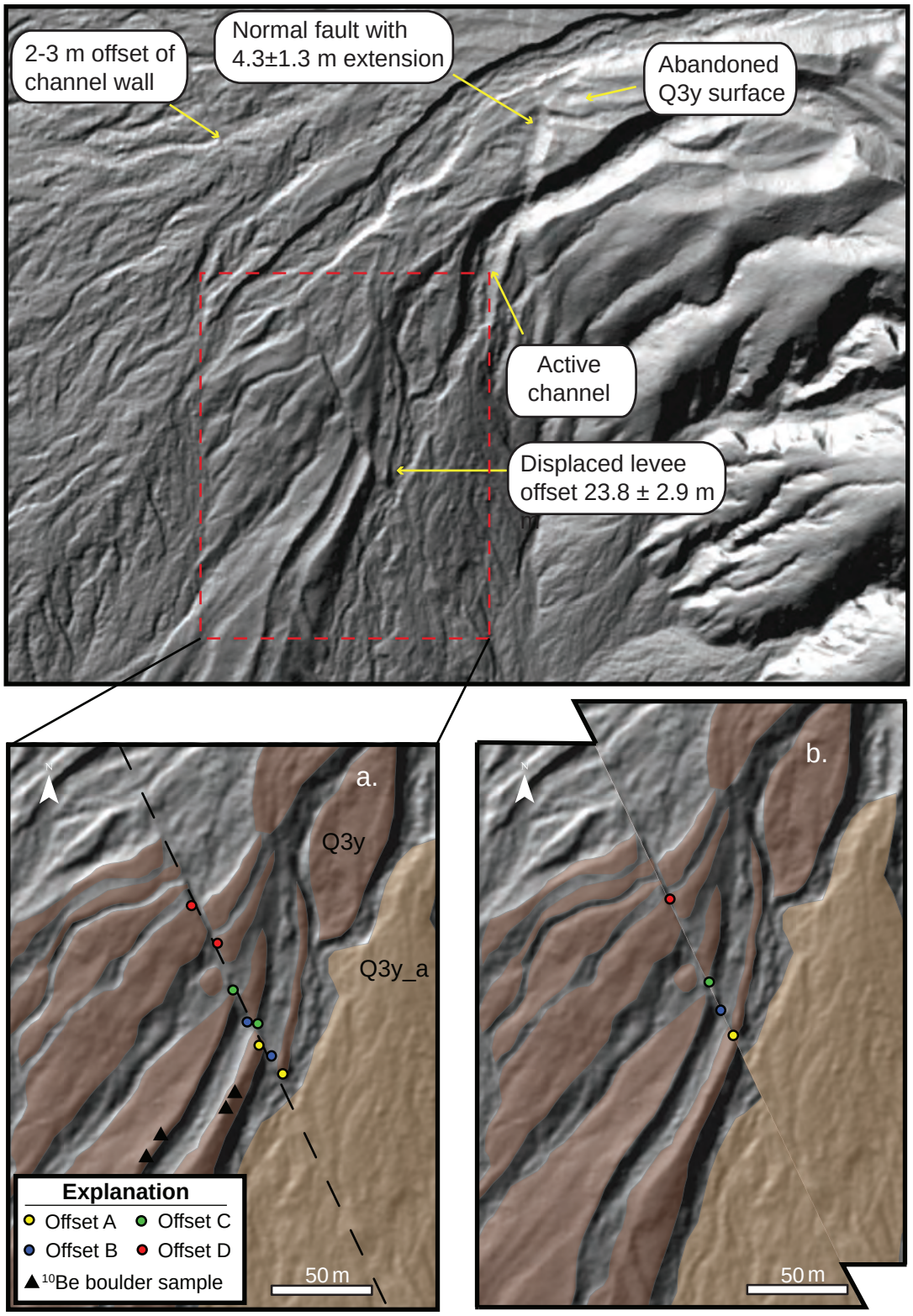

Figure 2-5: LiDAR image of the offset debris flow levees on the Q3y surface of the Manly Peak Canyon alluvial fan. Displacement magnitude of each piercing point used: A - 24.0 ± 4m levee crest; B - 24.2 ± 2m channel midpoint; C - 22.9 ± 3m levee edge offset; D - 23.9 ± 2m inside levee edge. (b) LiDAR image of the Manly Canyon alluvial fan restored 23.8 m to its original, pre-faulting configuration, with colored circles marking reconstructions from (a).

A series of distributed, northeast-striking normal faults are also present along the northwestern margin of the alluvial fan (Figure 2-4), where they displace surfaces mapped as Q2. These faults appear to merge with the Panamint Valley fault zone along the northern side of the fan complex, and Walker et al. (2005) interpret the NE-trending normal faults to be an extension of the Manly Pass fault zone, a low-angle normal fault system preserved along the western side of the Slate Range (Walker et al., 2005; Numelin et al., 2007) (Figure 2-1).

A series of low shorelines is present between the modern playa (elevation ~320 m) and ~350 m elevation on the northern and western sides of the alluvial fan complex. These shorelines are characterized by abrasional platforms, salt-shattered clasts, boulders with well-developed tafoni weathering, and constructional features such as beach ridges and spits. Rare lithoid tufa is associated with abrasional platforms and forms rinds developed on surface clasts. Although shorelines are well-developed on the Q2 deposits, they are not observed at similar elevations on the Q3y surface (Figure 2-4). This relationship, again recognized by Smith (1976), has led previous workers (Zhang et al., 1990) to infer that the debris-flows offset along the PVFZ must post-date the last withdrawal of the lake. Given uncertainties in the lacustrine history, most workers have assumed a rather large age range of 15-30 ka for the Q3y surface.

A series of high shorelines are also present north of the fan head between elevations of 550 – 600 m, where prominent abrasion platforms and wave-cut cliffs are developed in Plio-Quaternary alluvium along the range front (Smith, 1976). Given the absence of such features developed on the Q2 surface, I infer that the prominent Q2 fan

probably post-dates the last occupation of highstand shorelines (Gale stage of Smith, 1976), and is thus likely younger than 120 – 150 ka (Densmore and Anderson, 1997).

2.4 Happy Canyon Site

At Happy Canyon, several generations of alluvial fan complexes sourced from the Panamint Range on the eastern side of Panamint Valley are present. Many of these alluvial fans are cut by the PVFZ, though the amount of displacement on each fan surface varies depending on the age of the offset fan. I characterize the relative age of alluvial fan deposits at Happy Canyon (Figure 2-6), many of which appear to be Holocene in age, and map the distribution and displacement magnitude of faulting. I expand the alluvial fan characterization, with particular emphasis placed on the heavily faulted Q3o surface, which I use to constrain displacement to determine a slip rate at Happy Canyon. Because the surface is likely Late Pleistocene in age, I can compare the slip rate determined at Happy Canyon with the slip rate at Manly Peak Canyon over a similar timescale.

North of Ballarat, between Pleasant and Happy Canyons, the Panamint Valley fault zone takes a significant right-step, forming a broad embayment in the mountain front (Figure 2-6). Two primary sets of fault scarps trend northeast across this embayment. The southeastern scarp ranges in height from 60-80 m, and truncates a fan surface which I designate as Q3o. Along the southwestern part of this fault segment, a series of progressively offset surfaces with scarps ranging from 1 m to 20 m in height are developed in Late Pleistocene to Holocene fans. The northwestern of the two primary

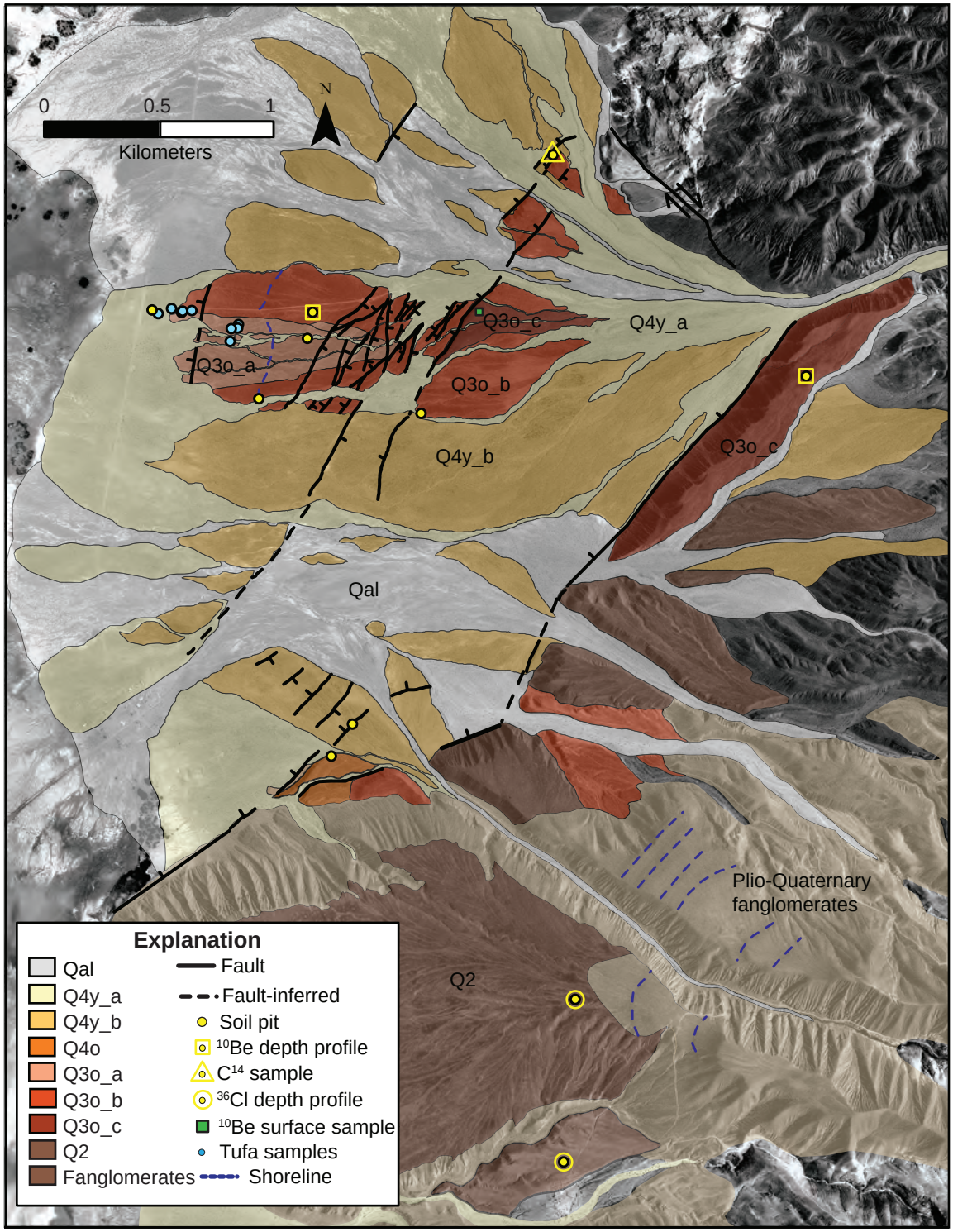

Figure 2-6: Digital Orthophoto of Happy Canyon slip-rate site with mapped faults and Quaternary alluvial fans. Broad embayment in the mountain front due to right step in PVFZ. Slip on NE-striking faults is pure dip-slip. NE-striking fault strands linked by NW-striking right lateral strike-slip fault, which is an example of slip partitioning. Locations of lithoid tufa samples, soil profiles, and cosmogenic depth profiles are shown. Results from depth profiles are pending.

fault systems has a complicated trace characterized by a single 3 - 4 m high east-facing scarp developed in Late Holocene fans, and by a distributed network of east- and west-facing scarps developed within Late Pleistocene surfaces along the Happy Canyon road (Figure 2-6). The two fault strands are linked by NW-trending bedrock along the range front, which exhibit shallowly plunging (<10˚) fault mullions and slickenlines toward ~300˚ (Kirby et al., 2004).

Displacement on both NE-trending faults is pure dip-slip, as indicated by displaced debris flow margins that exhibit no significant lateral separation (Figure 2-7). This is exhibited in several places by displaced debris flow margins with large boulders sitting on their respective fault scarp, indicating that faulting occurred after deposition of these debris flows (Fig. 2-7). These kinematic markers allow an opportunity to document extension direction along this part of the PVFZ, and are consistent with partitioning of oblique normal slip in a direction toward ~300˚ (Walker et al., 2005), sub-parallel to the long-term displacement vector in northern Panamint Valley (Burchfiel et al., 1987).

As noted above, for the slip rate determination I focus on the Q3o complex of alluvial fans. I refer to two sections of faulting on the Q3o complex of fans: the lower Q3o complex, and the Q3o bench. The lower Q3o complex of fans is located near the Happy Canyon road north of Ballarat, and is cut by the northwestern fault system at Happy Canyon, forming graben structures consisting of a series of southeast and northwest-dipping normal faults (Figure 2-6). Closer to the mouth of the canyon, a ~70 m high scarp cuts a similar surface, hereafter referred to as the Q3o bench.

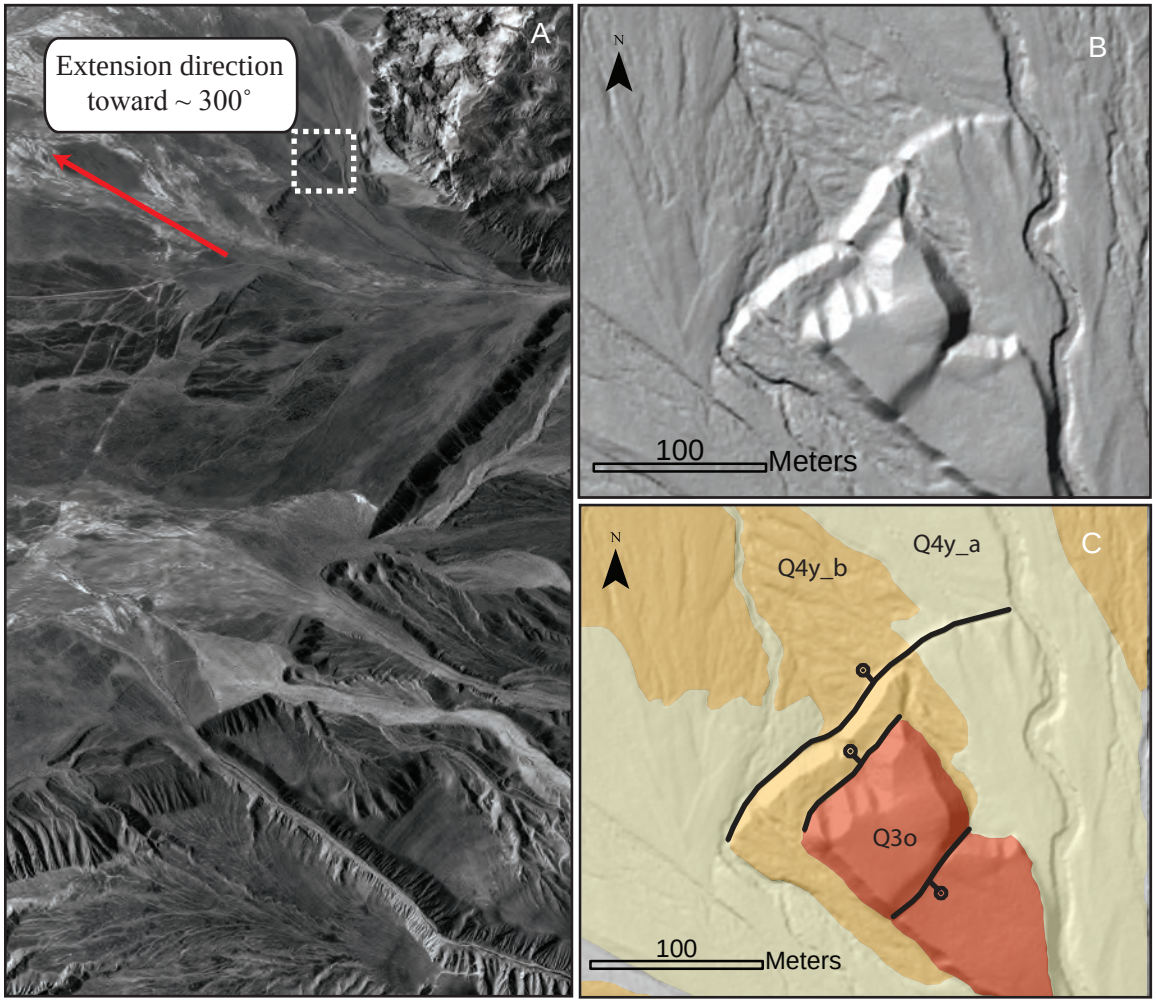

Figure 2-7: Example of fault displacement used to determine fault kinematics at Happy Canyon. A) Orthophoto of Happy Canyon. B) LiDAR image of fault scarps, and C) Fault and alluival fan map of alluvial deposits from the same image. D) Field photo of Q4y_a debris flow surface. Displacement is pure dip slip, as shown by the debris-flow margin offset with no lateral component. Boulders on the fault scarp indicate that faulting was post-deposition. Similar dip-slip offsets are seen in several places at Happy Canyon.

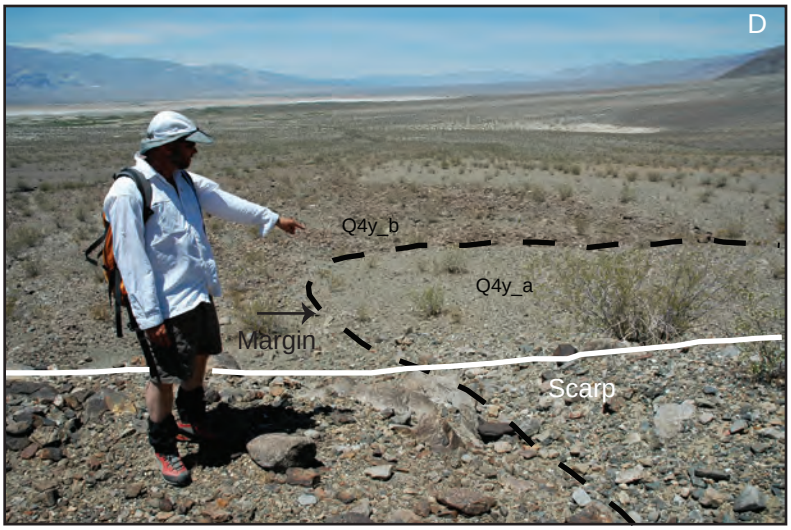

2.5 Reconstructing Fault Slip Using Geomorphic Markers

In order reconstruct fault slip from vertical displacement of alluvial markers, I assume normal fault angles of 60 ± 6°, consistent with faulting in unconsolidated alluvium in the near surface (Anderson, 1951). However, I recognize that relating displacement at the surface to fault slip at seismogenic depth is problematic (e.g., Fialko et al., 2005). This is particularly true if the active fault at depth cuts the brittle crust at relatively low angles (Burchfiel et al., 1987). Constraints presented in this thesis on surface displacement are therefore conservative estimates of true displacement along the fault at depth. Faults with lower angle geometries than 60° would result in higher total extension calculations, thus the extension rates presented here represent minimum rates.

2.5.1 Manly Peak Canyon

Previous determinations of the displacement of debris-flow levees south of Manly Peak Canyon vary widely from 17 - 27 m (c.f., Smith, 1976; Zhang et al., 1990). This discrepancy largely reflects the fact that the fault intersects the debris-flow channel at an oblique angle, and that there are subjective differences in the projection of both the debris flow levees and the trend of the strike-slip fault through this part of the fan complex. .

As noted above, there is also a normal fault at the range front that displaces the same, Q3y, alluvial deposits. In fact, the same channel system that provided a source for debris-flows farther down-fan is preserved in both the hanging wall and footwall of this fault strand (Figure 2-5). Together, these two fault strands extend to the south as individual scarps, eventually merging just north of Coyote Canyon (Figure 2-2). Thus, I

think that they together accomplish most of the slip along the PVFZ at this latitude. The separation of displacement into two fault strands, one a nearly dip-slip range front fault and the other a nearly pure strike-slip strand is an example of slip partitioning along the PVFZ. Similar geometries are observed in the Owens Valley (Le et al., 2007). Although whether faults partition slip depends largely on the strength of the fault system (e.g., Wesnousky and Jones, 1994), the close proximity of the two faults in this case make it likely that partitioning here is confined to the unconsolidated alluvium.

I reconstruct lateral slip along the strike-slip strand of the PVFZ using four individual markers: the two crests of the debris-flow levees that mark the channel, the midpoint of the channel itself, and the edge of a second inset debris-flow to the northwest. In each case, I incorporate uncertainties in the projection of each marker into the trace of the fault (details of the fault-slip reconstruction are described in Appendix A). I note here that the flat channel floor, and the presence of individual lobes of debris-flows at the downslope end of the channel (Figure 2-5), provide evidence that this channel was not subject to significant fluvial modification. Thus, the markers themselves were not likely subject to significant post-depositional modification (e.g., Cowgill, 2007), other than diffusive rounding and degradation of the levee crests. As such, the uncertainties in each case are rather small. Averaging all four offsets, I find the displaced debris flow levees to be offset by 23.8 m ± 2.9 (Figure 2-5) in a right lateral sense.

Using the surface of the Q3y fan as a marker of throw on the normal fault yields a throw of 7.4 ± 0.6 m and a heave of 4.3 ± 1.3 m (horizontal component) toward 270°, assuming an initial fault dip of 60 ± 6º. In order to estimate the total slip measured during the time interval since deposition of the Q3y unit, and for comparison to the

geodetic velocity field, I sum the horizontal components of each fault. The resultant vector yields a horizontal component of 26.5 ± 3.8 m in a direction toward 325°.

2.5.2 Happy Canyon

Here, I reconstruct normal slip along the dip-slip strands of the PVFZ using the Q3o fan complex as a marker of displacement. A brief description of the fault reconstruction method is outlined below, with a detailed description of the method in Appendix A. The method I used for fault slip reconstruction is described in detail in Appendix A and C of Thompson et al.'s (2002) paper on slip rates across the Kyrgyz Tien Shan. I summarize the method used and representation and calculation of associated uncertainties first outlined by Thompson et al. (2002).

To reconstruct fault slip on an alluvial fan surface, I consider the case of a fault or multiple faults that cut an originally planar alluvial fan surface. I surveyed the present-day abandoned alluvial fan surfaces normal to the structural trend to reconstruct the vertical displacement across the normal faults. The survey represents points along the hanging wall surface slope, footwall surface slope, and across the fault that are then used to calculate hanging wall ($y_{hw} = m_{hw}x + b_{hw}$) and footwall ($y_{fw} = m_{fw}x + b_{fw}$) surfaces using least squares linear regression, where tangent of the alluvial fan dip, $\tan \alpha = m$ (Figure 2-8).

For the displacement reconstructions, I assume an initial fault dip angle (α) of 60° and project y_{hw} and y_{fw} to intersection points with the initial fault surface (x_{hw},y_{hw}; x_{fw}, y_{fw}), which is calculated using the midpoint of the present-day scarp face and a 60° slope.

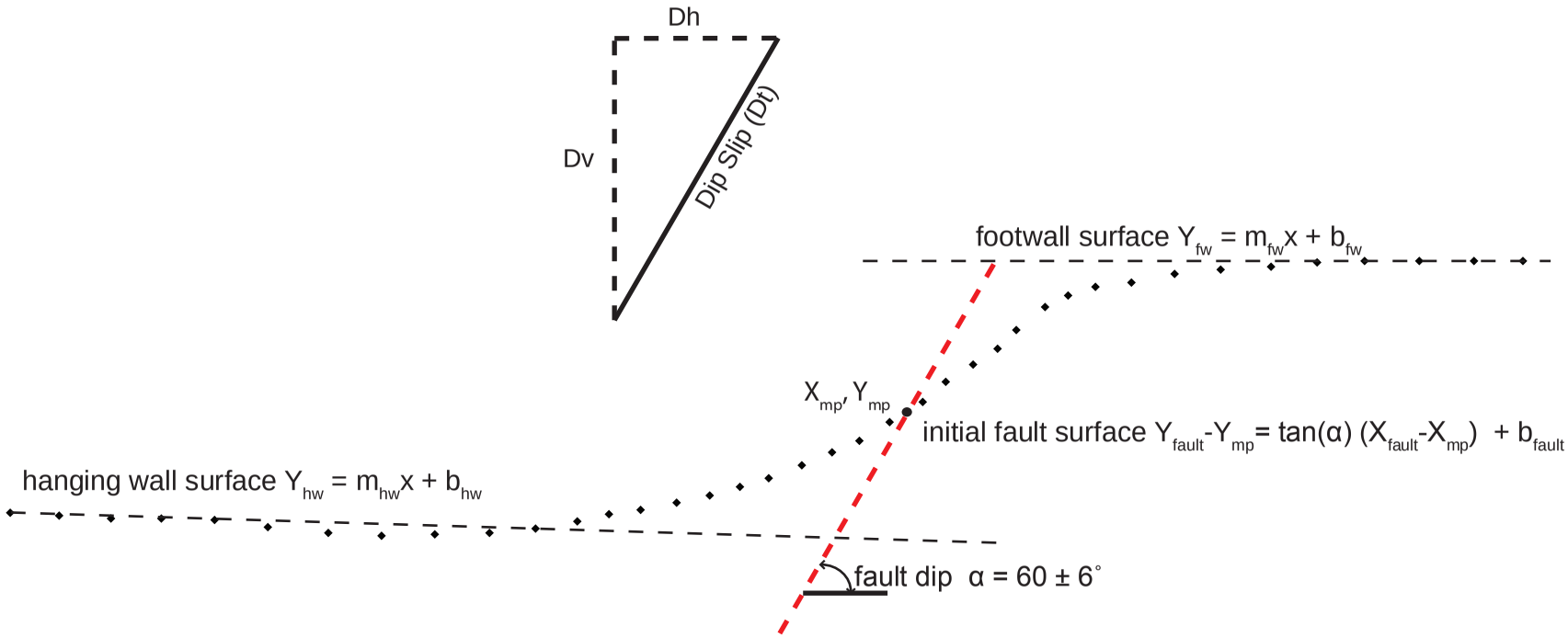

Figure 2-8: Analysis of a faulted alluvial fan, showing fault slip reconstruction from raw topographic dGPS ground survey profile (solid dots). The modeled hanging wall and footwall surfaces (black dashed lines) represent least squares regressions of surface slope from survey points used to project the trace of the surfaces before scarp diffusion/erosion. Red dashed line represents scarp surface, centered at X_{mp}, Y_{mp}, which was determined in the field, where possible. Parameters allowed to vary in the Monte Carlo simulations were hanging wall surface, footwall surface, and fault dip (60 ± 6˚). From these, we calculated the total displacement (D_t), vertical displacement component (D_v), and horizontal displacement component (D_h).

Total displacement (D_t), vertical displacement (D_v), and horizontal displacement (D_h) are calculated for each fault, then are summed together to gain the total amount of vertical and horizontal displacement on the alluvial fan surface (Figure 2-8).

Several sources of error exist during the fault slip reconstruction calculations used in this thesis, as outlined above. To account for the uncertainties in fault slip calculations, I used Crystal Ball to run Monte Carlo simulations, which take into account the errors associated with initial fault angle and linear regressions of the hanging wall and footwall surfaces in the scarp profile. I considered uncertainties in initial fault dip to be 60± 6°, and uncertainties in slope (m) and intercept (b) based on least squares method for linear regression. The Monte Carlo simulation ran ten thousand calculations, with each trial simulation sampling a variety of probability distributions that represent uncertainty for each assigned variable. Because each parameter is characterized by a measurable mean and standard error, I used normal distributions to describe the probability density functions from the simulations.

Differential GPS ground surveys and LiDAR digital topographic analysis perpendicular to the strike of eleven fault scarps cutting the lower Q3o surface yield a total extension of 14.8 ± 1.9 m. LiDAR digital topographic analysis perpendicular to the strike of the Q3o bench yields 41.2 ± 10.1 m extension and a vertical displacement of 68.1 ± 2.0 m. Summing the extension components of the lower Q3o surface and the Q3o bench yields a total extension magnitude of 56.0 ± 10.3 m (Figure 2-9).

In the case of the Q3o bench, the initial hanging wall surface is unknown because it is buried by younger alluvial deposits. Therefore, the measured vertical displacement of the Q3o bench provides only a minimum estimate due to projection uncertainties, and

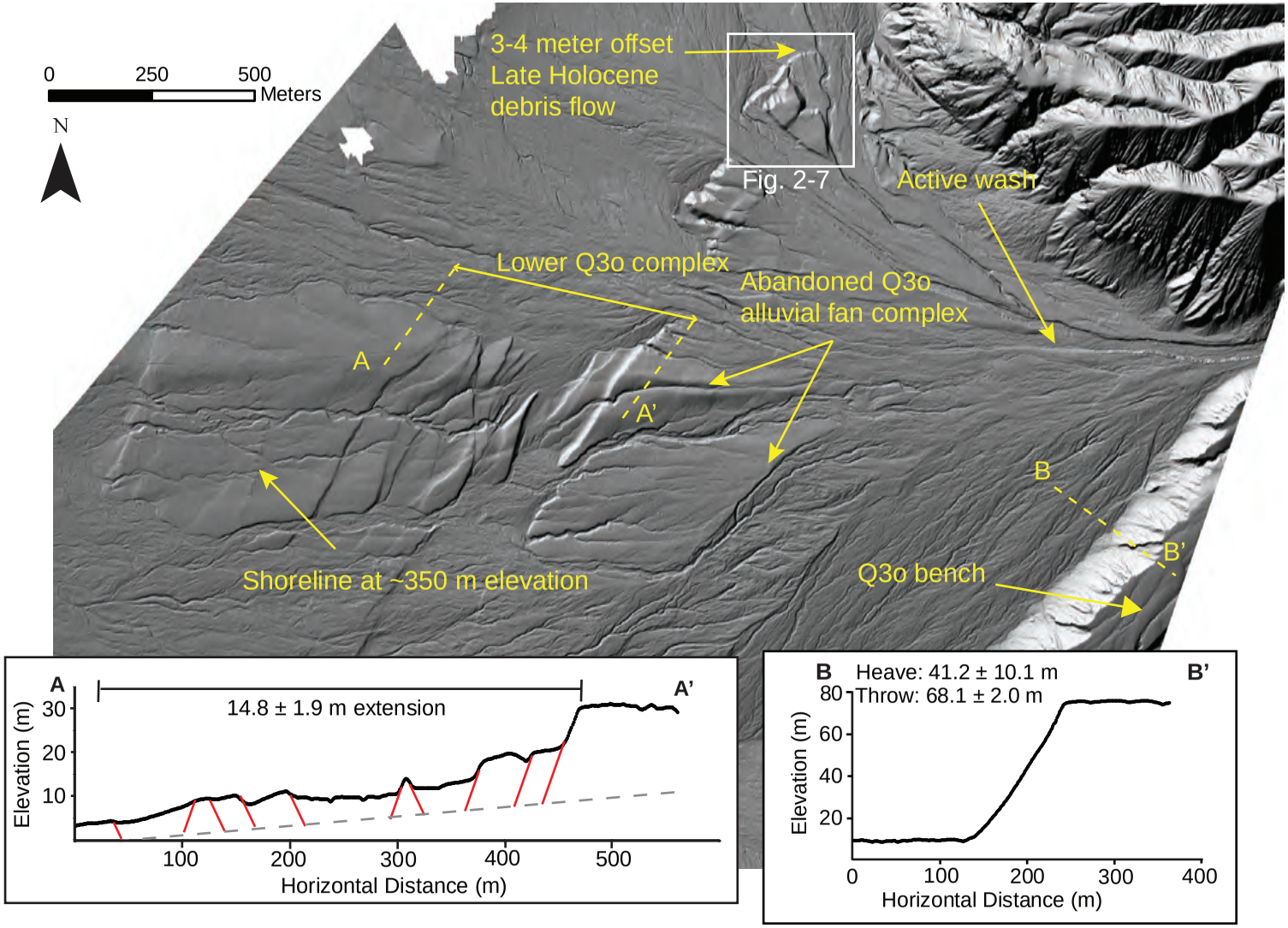

Figure 2-9: LiDAR image of Happy Canyon slip rate site showing faulted alluvial fan surfaces used for displacement calculations. Topographic transects from LiDAR DEM shown. Heave and throw on Q3o bench represent minimum displacements.

the resulting fault slip reconstructions for both the amount of heave and throw on the Q3o bench are minimum values.

2.6 A Soil Chronosequence in Panamint Valley

In order to determine the age of the Q3y fan surface and associated debris-flow levees at Manly Peak Canyon and the Q3o fan surface at Happy Canyon, I undertook a multi-pronged approach to developing an absolute chronologic framework for Late Pleistocene – Holocene deposits along the Panamint Valley range front. First, I utilized radiocarbon and cosmogenic radionuclide (^{10}Be) dating of fan surfaces at several locations along the range front. These included a young debris-flow deposit near Happy Canyon with embedded juniper logs, lacustrine tufa from shoreline deposits at Happy Canyon and Manly Peak Canyon, and a ^{10}Be depth profile from the Q2 surface at Manly Peak Canyon. I characterized the degree of soil development beneath well-preserved alluvial surfaces at these sites to develop a locally-calibrated soil chronofunction that relates the degree of soil development to age (e.g., Harden, 1982; Slate, 1999), and used this to estimate the age of the Q3y and Q3o surfaces.

Soils were characterized in 25 individual soil pits distributed across alluvial fan surfaces between Manly Peak and Happy Canyons (Figure 2-10). The soil was logged, described and sampled following procedures outlined in Soil Survey Staff (1993). The degree of soil development was quantified using the Soil Development Index (SDI) procedures according to Harden (1982) and Taylor (1988). Calculation of SDI values is based on a conversion of soil morphology (i.e., color, structure) into numerical data to

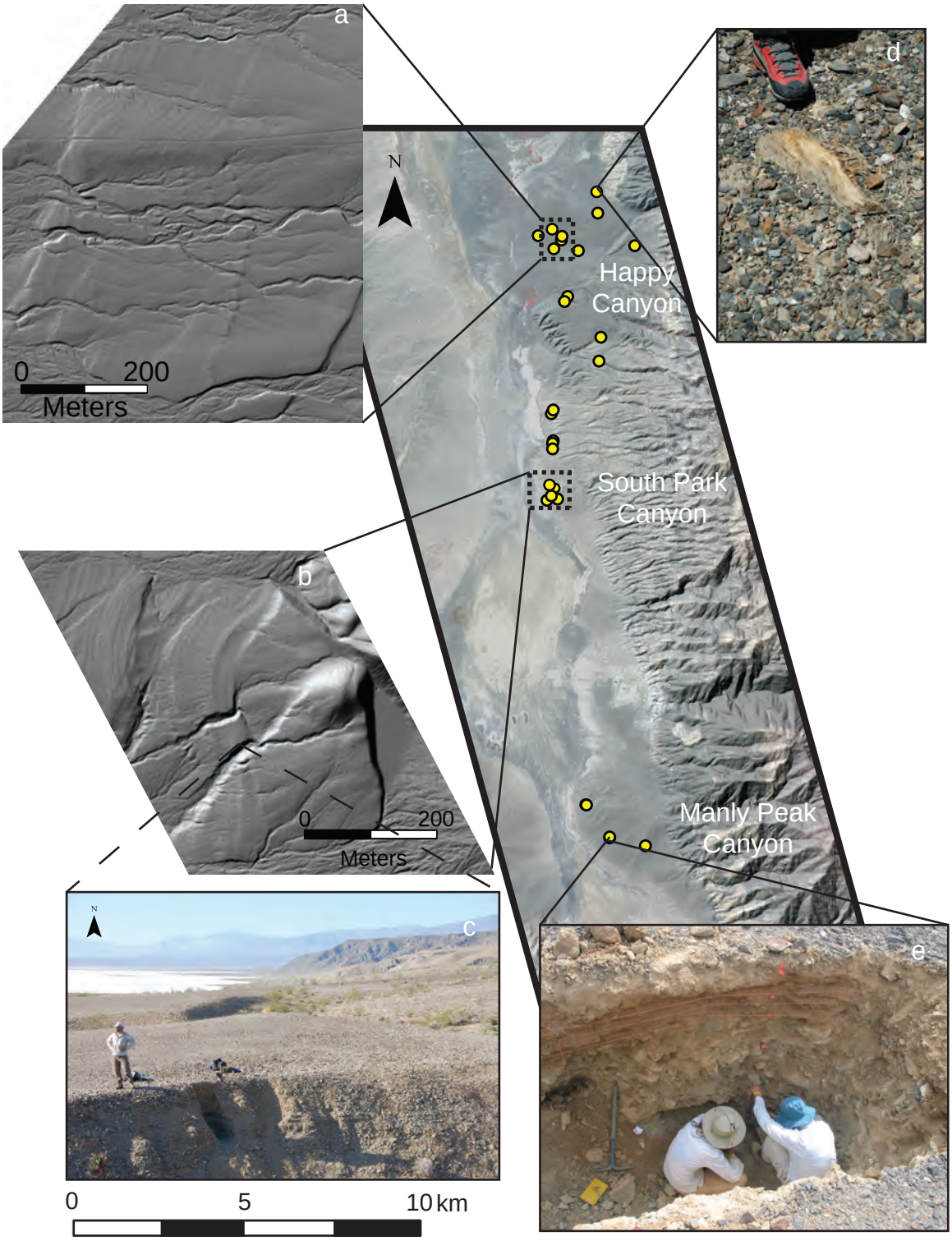

Figure 2-10: Location of 25 soil pits (yellow circles) along the eastern side of Panamint Valley (same extent as Figure 2-2). a) LiDAR image of low elevation shorelines at Happy Canyon. b) LiDAR image of low elevation shorelines at South Park Canyon. c) Beach ridge at South Park Canyon and PAN-23 soil profile. d) Juniper log embedded in young debris flow at Happy Canyon. e) ^{10}Be Depth profile (PAN-3) pit at Manly Peak Canyon.

enable semiquantitative comparisons of the degree of soil development. Points are assigned to each property based on the difference between the described soil property and the parent material. Points for each property are normalized to a percentage scale of maximum property development based on comparison of each property to a published or conceptual maximum value of development for each particular property. Profile properties of rubification, texture, dry and moist consistency, and soil carbonate were used to derive the results reported here. Maximum soil property values from Taylor (1988) were used to normalize soil property values in this study. Normalized property values are summed for each horizon and averaged yielding a Horizon Development Index (HDI) value that provides an estimate of overall horizon development relative to a conceptual idea of maximum possible horizon development. HDI values are multiplied by horizon thickness and summed for each profile yielding a Profile Development Index (PDI) value for that profile. PDI values provide a means of relative comparison among soils within a given sequence and, when calibrated to independent chronologic constraints, can be used to develop a soil chronofunction. The chronofunction can be inverted to provide soil age estimates based on calculated PDI values, with ages reported along with 25% error. Of the 25 soil pits, 6 were used in the development and calibration of a soil chronosequence. Here, I describe the geomorphic context and chronology at each of the calibration sites.

2.6.1 Radiocarbon ^{14}C Age at Happy Canyon

Near the mouth of Happy Canyon, a matrix-rich debris-flow deposit is preserved near the northern side of the alluvial fan complex. This flow forms a 0.5 – 1 m thick carapace atop a boulder-rich Holocene fan surface with well-developed bar and swale topography. I recovered woody debris from several juniper logs embedded within the debris-flow deposit (Figure 2-10). Radiocarbon ages from the outer portions of the wood constrain the debris-flow to be younger than ~600 - 700 Cal yr BP. Given that the current range of juniper is typically above ~1500 m elevation in this region today, this wood must have been incorporated into the flow somewhere near the source, and thus places a maximum constraint on the age of the deposit. Soil development within the debris-flow is generally quite weak, with only incipient horizonation (Table 2.2). The soil has a Profile Development Index of 0.5.

2.6.2 Radiocarbon ^{14}C Ages of Low Elevation Shorelines

As noted above, numerous exposures of Late Pleistocene alluvial fans on the eastern side of Panamint Valley exhibit wave-cut benches at elevations between ~320 m and ~350 m that reflect occupation by a relatively recent lake in Panamint Valley. I characterized these deposits and geomorphic features at three locations along the eastern range front. Mapping and topographic characterization were aided by high-resolution digital topography generated from airborne LiDAR, and soil characterization was conducted at both abrasion platforms and constructional beach ridges.

Table 2.2. SUMMARY OF MORPHOLOGICAL AND TEXTURAL CHARACTERISTICS OF SOILS DEVELOPED IN PANAMINT VALLEY, CA

Site Location (UTM,Elevation)	Horizon[a]	Depth (cm)	Munsell Color dry matrix	Texture[a]	Structure[a]	Consistency[a] dry matrix	Particle size (<2 mm)[b] Sand	Silt	Clay	PDI Value	Deposit Age
PAN-6	Avj	0-3	10YR 6/4	gsl	m/1m-cpl	sh	52	41	7	**0.51**	0.6 ka
	ACk	3-14	10YR 6/3.5	gsl	m/1msbk	sh	48	45	7		Juniper log
11 S 481785, 3399179	CA	14-40	10YR 6/4	vgsl	m	sh	52	42	7		
Elevation: 413 m	Cy1	40-83	10YR 5.5/3	gsl	m	sh	48	45	7		
	Cy2	83-105	10YR 5.5/3	vgsl	m	sh-h	50	44	7		
PAN-17	Avy	0-3	10YR 5.5/3	sl	2m-cpr:1mpl	sh-h	58	24	18	**9.93**	12.5 ka
	Avky	3-10	10YR 5/3	sl	2-3cpr	sh-h	63	16	20		shoreline
11 S 479881, 3399107	ABky	10-16	10YR 5/4	gl	1mpr/1msbk	so	48	38	14		
Elevation: 324 m	Bwky1	16-38	10YR 5/4	gsl	1msbk/m	sh-so	56	39	5		
	Bwky2	38-63	8.75YR 6/3	gsl	1msbk/sg	so-lo	57	36	7		
	Cky	63-80	10YR 6/3	gsl	m	h-sh	49	44	7		
	Ckyb1	80-120	10YR 7/3	vgsl	m	so-sh	49	43	8		
	Ckyb2	120-155	10YR 6/3	exgsl	sg	lo	48	44	7		
PAN-21	Av	0-5.5	10YR 6/4	l	3c-mpr:2-1c-mpl: 2msbk	sh	44	41	15	**8.66**	12.5 ka
	Btky	5.5-18	10YR 6/4	gsl	2-1vc-cpl:2-1m-fsbk	so-sh	56	31	13		shoreline
11 S 480137, 3974033	Bky1	18-36	10YR 6.5/4	vgs	m-sg	so-lo	90	9	1		
Elevation: 342 m	Bky2	36-67	10YR 6/3	exgls	m	sh	76	21	3		
	Bky3	67-84	10YR 6/4	exgls	m	so	79	18	3		
	BCky	84-98	10YR 6.5/3	vgls	m-sg	lo-so	84	13	2		
	CBky	98-115	10YR 6/3	vgls	sg	lo	67	27	6		
	Ck1	115-153	10YR 7/3	vgls	sg	lo	79	19	3		
	Ck2	153-205	10YR 6.5/3	vgls	sg	lo	81	16	3		
PAN-22	Av	0-4.5	10YR 7/4	sil	2-3c-mpr:1-2cpl	sh-h	31	52	17	**7.20**	12.5 ka
	Bwky1	4.5-14	8.75YR 6/4	gsl	2-1vc-cpl:2msbk	sh-so	53	37	11		shoreline
11 S 481328, 3983157	Bwky2	14-27	7.5YR5/4	vgsl	sg	lo-so	77	17	6		
Elevation: 320 m	Bwky3	27-44	8.75YR5/4	vgls	sg	lo	89	7	3		
	BCky	44-72	8.75YR5/4	exgsl	sg	lo	90	7	3		
	Cky1	72-91	10YR 6/4	exgls	sg	lo	84	13	3		
	Cky2	91-121	10YR 6/4	exgsl	sg	lo	94	4	2		

Note: Location in WGS84 datum; Elevation in meters above mean sea level.

[a] Notations from Soil Survey Staff (1998) and Birkeland (1999).

[b] Particle size distribution measured using laster light scattering method of Gee and Or (2002) for all soils, except for Muggins Mountains site where the pipette method after removal of calcium carbonate and soluable salts by the sodium acetate digestion method was used.

Table 2.2 Continued. SUMMARY OF MORPHOLOGICAL AND TEXTURAL CHARACTERISTICS OF SOILS IN PANAMINT VALLEY, CA

Site Location (UTM, Elevation)	Horizon[a]	Depth (cm)	Munsell Color dry matrix	Texture[a]	Structure[a]	Consistency[a] dry matrix	Particle size (<2 mm)[b] Sand	Silt	Clay	PDI Value	Deposit Age[c]
PAN-23	Av	0-4	10YR 6/4	l	2-1c-mpr:2-1mpl/2-1msbk	sh	39	46	15	**8.25**	12.5 ka shoreline
	Bwky1	4-10	10YR 6/4	gl	2-1msbk:	so	48	43	10		
11 S 480460, 3983190	Bwky2	10-26	8.75YR 6/4	vgl	1msbk/m	so	43	46	10		
Elevation: 347 m	Bwky3	26-44	8.75YR 6/4	vgsl	1msbk/m	so	51	43	6		
	BCky	44-70	10YR 6/4	exgls	sg	lo	82	15	3		
	Cky1	70-85	10YR 6/4	exgls	sg	lo	82	15	3		
	Cky2	85-101	10YR 6/3	s	sg	lo	96	3	1		
	Cky3	101-131	10YR 5/4	exgls	sg	lo	76	20	4		
PAN-20	Av	0-4.5	10YR 6/4	sil	2cpr:1cpl	sh	32	53	15	**9.39**	Preferred age 11.6 - 13.9 ka
	Bwky1	4.5-15	10YR 6/4	gsl	1m-fsbk/sg	sh-lo	59	32	9		
11 S 483091, 3972814	Bwky2	15-32	8.75YR 6/4	vgsl	1msbk/m	sh-so	68	25	7		
Elevation: 378 m	Bky	32-52	10YR 6/4	vgsl	m	so-sh	69	27	4		
	BCky	52-72	10YR 6/4	exgsl	m	sh-so	73	23	4		
	Ck1	72-105	10YR 6/4	vgsl	m	sh-so	73	23	3		
	Ck2	105-145	10YR 6/3	vgsl	m	sh-so	61	34	5		
PAN-3	Av1	0-4	10YR 6/4	l	3cpr:1-2pl	sh	36	48	16	**31.06**	86.5 ka, ^{10}Be depth profile
	Av2	4-10	10YR 6/4	l	2-3pr:1-2c-mpl	sh	47	36	17		
11 S 482018, 3973070	Btky1	10-32	10YR 5/4	gl	1-3c-mpl:1-2m-fsbk	so-sh	52	31	17		
Elevation: 354 m	Btky2	32-49	8.75YR 4/4	vgl	1-2m-fsbk	h-sh	nd	nd	nd		
	Btky3	49-76	10YR 5/4	vgsl	m/1msbk	h	70	26	4		
	Bky	76-104	10YR 5/3	vgsl	m	h	69	28	3		
	BCky	104-137	10YR 6/4	vgsl	m	lo	73	24	3		
	Cky1	137-152	10YR 6/3	vgsl	sg	lo	89	9	2		
	Cky2	152-179	10YR 6/3	gsl	m	sh	78	18	3		

Note: Location in WGS84 datum; Elevation in meters above mean sea level.

[a] Notations from Soil Survey Staff (1998) and Birkeland (1999).

[b] Particle size distribution measured using laster light scattering method of Gee and Or (2002) for all soils, except for Muggins Mountains site where the pipette method after removal of calcium carbonate and soluable salts by the sodium acetate digestion method was used.

[c] Chronofunction estimates the age of the PAN-20 deposit to be 15.4 ± 3.8 ka.

I dug pits and characterized soils at three separate locations along the ~340 – 350 m shorelines, at Happy Canyon, South Park Canyon, and Manly Peak Canyon (Figure 2-10). At Happy Canyon, a succession of wave-cut benches is clearly visible in the LiDAR image, with the highest of these shorelines present at ~350 m. Shoreline features are only developed across older alluvial surfaces preserved along the axis of the fan and are not developed in alluvial fan deposits to the north and south. The highest elevation shoreline is associated with a 0.5 – 1 m high beach berm, composed of well-rounded and sorted pebbles. Clasts in the relict alluvium beneath the bar are extensively fractured, consistent with salt shattering during or after lacustrine occupation. Subtle abrasion platforms and benches are inset beneath the bar and likely reflect recessional stillstands during drawdown of the lake. Many of these platforms exhibit scattered mounds of lithoid tufa in growth positions. At the western extent of the fan surface, near the playa, a 4 – 5 m high fault scarp cuts both the fan surface and the shorelines.

Just south of South Park Canyon, a series of wave-cut, low shorelines are present between the modern playa and ~350 m elevation. The series of shorelines closer to the playa are characterized by broad, abrasional platforms, which extend laterally for many tens of meters. The highest shoreline (350 m) is associated with a well-developed wave-cut cliff (Figure 2-10); inset beneath this cliff is an arcuate beach ridge composed of >3 m of rounded gravel. I characterized soils in several of these features, including both erosional and constructional features (PAN-21 and PAN-22: abrasional platforms; PAN-23: beach ridge; Figure 2-11; Table 2.2). Lithoid tufa deposits, present at Manly Peak and Happy Canyons, are absent at South Park Canyon.

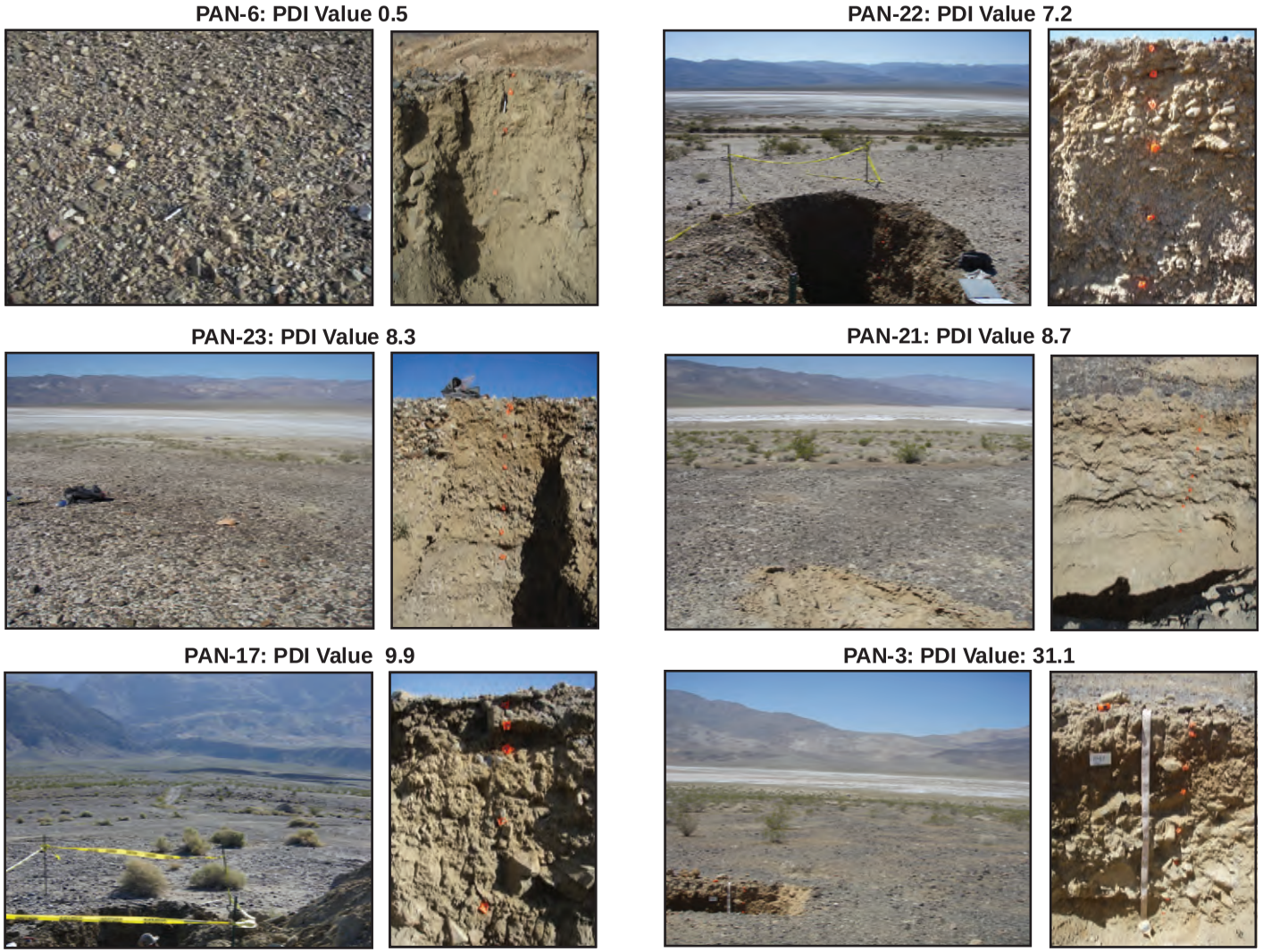

Figure 2-11: Field photos of soil calibration sites with accompanying soil profiles. Profile Development Index (PDI) values listed with site name. See Table 2.2 for soil descriptions for each location.

In order to determine the timing of development of these shoreline features, I collected lithoid tufa found in growth position on abrasion platforms and subjected them to radiocarbon dating at the AMS facility at the University of Arizona. Conventional ^{14}C dates reported in this study have been converted to calibrated ages using the CALIB v. 5.0.2 program (Stuiver and Reimer, 1993) with the INTCAL04 data set (Reimer et al., 2004). To minimize the possibility that tufas may have exchanged carbon with the atmosphere during post-depositional weathering or alteration, each sample was subjected to progressive leach steps in a weak acid. A detailed description of analytical methods can be found in Appendix B. Uncalibrated ^{14}C ages are progressively older for each step, suggesting that the oldest age reflects the least altered material near the core of the sample. Thus, for all 14 samples, I consider the third leach step as a more reliable estimate of the age of tufa precipitation. Although tufa is also susceptible to contamination with detrital carbon, and may potentially yield erroneously old ages (e.g., Bischoff et al., 1993), the relatively tight clustering and young age of the samples suggest that this is likely not a significant problem in these samples.

The results from fourteen lacustrine tufa samples at Happy Canyon and Manly Peak Canyon yield a mean age of 12,500 ± 1400 Cal years BP (Table 2.3). The tight clustering of these ages between 10 – 14 ka suggests that shoreline features preserved between 320 – 350 m in Panamint Valley reflect occupation by a shallow lake during the Late Pleistocene (MIS 2). This is consistent with a brief highstand in Searles Valley during this time (Smith and Street-Perrot, 1983) that probably delivered water from the Owens River system to southern Panamint Valley. Although reservoir effects associated with a lake in Panamint Valley are unconstrained, I acknowledge it is possible that these

Table 2.3. RADIOCARBON DATES ON TUFA DEPOSITS FROM SITES IN THIS STUDY IN PANAMINT VALLEY, CA

Sample and leach number[1]	Material Dated	Sample Location	Elevation (m)	Radiocarbon date[2] (yr BP)	δ^{13}/δ^{12} (‰)	Calibrated Date[3] (Cal yr BP)
X14413C	Tufa	PV-T1;	327	10860 ± 64	+ 1.9	**12,881-12,826**
X14413B				10904 ± 61	+ 1.9	
X14413A		Lower HC		10529 ± 73	+ 1.5	
X14414C	Tufa	PV-T2;	330	11427 ± 82	+ 4.1	**13,347-13,220**
X14414B				11236 ± 62	+ 3.8	
X14414A		Lower HC		9867 ± 55	+ 3.9	
X14415C	Tufa	PV-T3;	332	12140 ± 120	+ 3.4	**14,098-13,879**
X14415B				11256 ± 62	+ 3.6	
X14415A		Lower HC		9118 ± 57	+ 3.4	
X14416C	Tufa	PV-T4;	332	12324 ± 67	+ 3.4	**14,464-14,073**
X14416B				11808 ± 61	+ 3.5	
X14416A		Lower HC		10387 ± 57	+ 3.8	
X14417C	Tufa	PV-T5;	333	9741 ± 57	+ 3.2	**11,219-11,171**
X14417B				9463 ± 57	+ 3.1	
X14417A		Lower HC		7071 ± 52	+ 3.3	
X14418C	Organic	PV-T6;	344	10994 ± 89	- 0.5	**12,965-12,869**
X14418B				10745 ± 67	+ 0.3	
X14418A	material	Upper HC		9972 ± 69	+ 0.8	
X14419C	Tufa	PV-T7;	343	11387 ± 63	+ 3.5	**13,307-13,199**
X14419B				11024 ± 67	+ 3.7	
X14419A		Upper HC		10191 ± 57	+ 3.7	
X14420C	Tufa	PV-T8a;	342	9081 ± 55	+ 3.6	**10,250-10,215**
X14420B				8317 ± 59	+ 3.9	
X14420A		Upper HC		7073 ± 52	+ 3.5	
X14421C	Tufa	PV-T8b;	342	11673 ± 66	+ 4.3	**13,626-13,423**
X14421B				12107 ± 71	+ 4.1	
X14421A		Upper HC		11340 ± 64	+ 4.2	
X14422C	Tufa	PV-T8c;	342	12361 ± 77	+ 3.9	**14,612-14,120**
X14422B				11811 ± 94	+ 3.9	
X14422A		Upper HC		10572 ± 62	+ 3.8	
X14423C	Tufa	PV-T9;	342	10932 ± 65	+ 4.3	**12,918-12,851**
X14423B				10790 ± 65	+ 3.9	
X14423A		Upper HC		9342 ± 58	+ 4.0	
X14424C	Tufa	PV-T10;	338	11137 ± 82	+ 1.7	**13,108-12,955**
X14424B				11006 ± 85	+ 1.6	
X14424A		MC		9876 ± 61	+ 1.5	
X14425C	Tufa	PV-T11;	338	8909 ± 61	+ 3.3	**10,083-9917;**
X14425B				9355 ± 63	+ 3.3	
X14425A		MC		8490 ± 59	+ 3.3	**10,176-10,115**
X14426B	Tufa	PV-T12;	338	9088 ± 63	+ 3.5	**10,254-10,215**
X14426A		MC		8213 ± 71	+ 3.4	

Note: Radiometric and accelerator mass spectrometry (AMS) dates provided by NSF Arizona MS Laboratory

[1] A,B, and C refer to the leach step taken to minimize the amount of contamination from atmospheric carbon.

[2] Radiocarbon date ± 1σ using Libby half-life of 5,568.

[3] Radiocarbon date is calibrated at ± 2σ using CALIB v 5.0.2 program (Stuiver and Reimer, 1993) with the INTCAL04 data set (Reimer et al., 2004).

radiocarbon ages could be too young if there was a significant reservoir of unsupported carbon in the lake (e.g., Lin et al., 1998).

2.6.3 ^{10}Be Depth Profile on the Q2 Surface

As described above, the prominent Q2 surface on the Manly Peak fan extends from nearly the playa floor at ~320 m to nearly ~400 m elevation. The surface sits well below the Gale stage shorelines (Smith, 1976) at ~550 – 600 m on the rangefront, but is cut by a sequence of low shorelines (dated to MIS 2) along its northwestern margin (Figure 2-4). The absence of shoreline features higher than 350 m on this fan suggest that the fan postdates the last occupation of high shorelines in the valley (120-150 ka; Densmore and Anderson, 1997) but predates the low shorelines (12,500 ± 1400 cal yrs BP). To better refine the age estimate on this surface, I collected a depth profile of five samples for ^{10}Be dating on the Q2 surface at Manly Peak Canyon, with the deepest sample at ~1.5 m. Samples were prepared at University of Kansas using standard quartz separation methods from whole rock samples followed by successive etching to remove any remaining feldspar, meteoric components, and weathering products. Be was extracted from the pure quartz by anion and cation exchange chromatography. Samples were then sent and analyzed for ^{10}Be concentrations by accelerator mass spectrometry (AMS) at Purdue Rare Isotope Measurement Laboratory (PRIME Lab). My interpretation of the age of the surface is based on a Monte Carlo ^{10}Be depth profile simulation model by Hidy et al. (in review), which allows site-specific geologic observations to be incorporated to better constrain exposure age, erosion rate, and inheritance.

Surface age and uncertainty are reported on the Manly Peak Canyon Q2 fan (Figure 2-12). At 2σ, 500,000 curves were fit to the ^{10}Be concentration data, yielding a minimum surface age of 72.1 ka. The optimal exposure age produced by the model, based on the parameters yielding the best fit (lowest $\chi 2$ value), is 90.3 ka. However, I report the modal age value as the most appropriate exposure age, based on the highest frequency peak of all the profiles generated, which yields an age of 86.5 +19.2/-14.4 ka at 2σ (Figure 2-12). The modal inheritance value of $1.01*10^5$ atoms/g, while high, is reasonable compared to other inheritance values measured in similarly arid environments in the Mojave Desert. A full explanation of the depth profile simulation model (Hidy et al., in review) is presented in the methods section in Appendix C.

2.6.4 Evaluation of Soil Chronosequence in Panamint Valley

A total of eight soil profiles on surfaces with radiometric age control were used as calibration soils for the Profile Development Index (PDI) chronofunction of soils in Panamint Valley. In addition to the sites described above, I included two dated Late Holocene surfaces from near Yuma, Arizona (Bacon et al., in review). This site has a similar modern climate regime to Panamint Valley, and fills in a critical age range on the chronsequence. Linear regression of soil PDI values versus age yields an empirical chronofunction that describes how soil characteristics change with time (Figure 2-13). The high correlation coefficient ($r^2 = 0.97$) suggests that most of the variance in the, admittedly sparse, data is captured by this regression. For instance, PDI values from soils

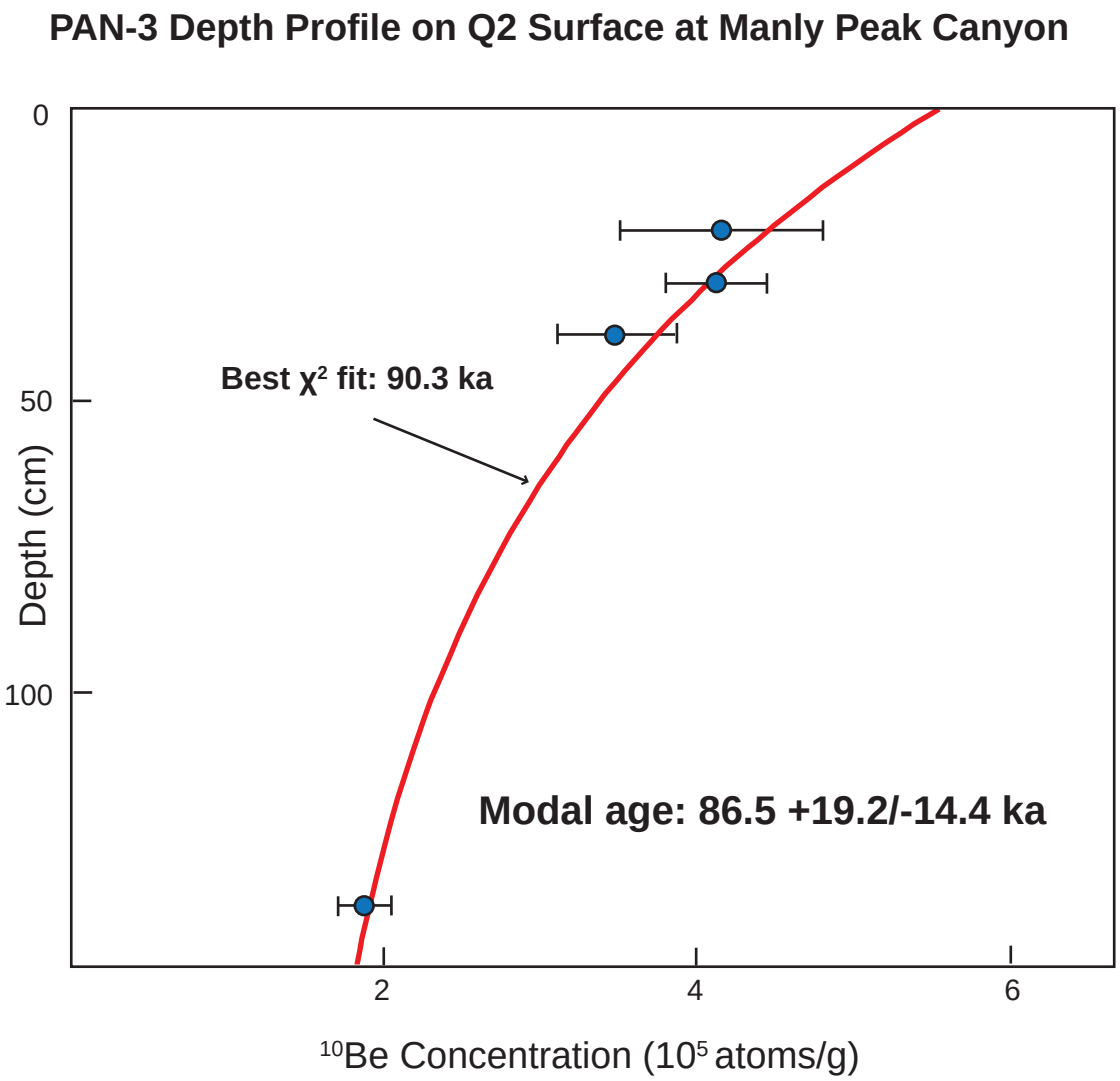

Figure 2-12: Fit of calculated ^{10}Be concentration with depth to Manly Canyon (Q2 surface) PAN-3 depth profile using a ^{10}Be depth profile simulation model (Hidy et al., in review). Best fit (lowest χ^2 value) curve shown in red, yielding an age of 90.3 ka. Modal age is result of highest frequency peak from results of 500,000 curves fit to the ^{10}Be concentration data. I use the modal value of 86.5 +19.2/-14.4 ka for the age of the Q2 surface. A more detailed description of the model is included in Appendix C.

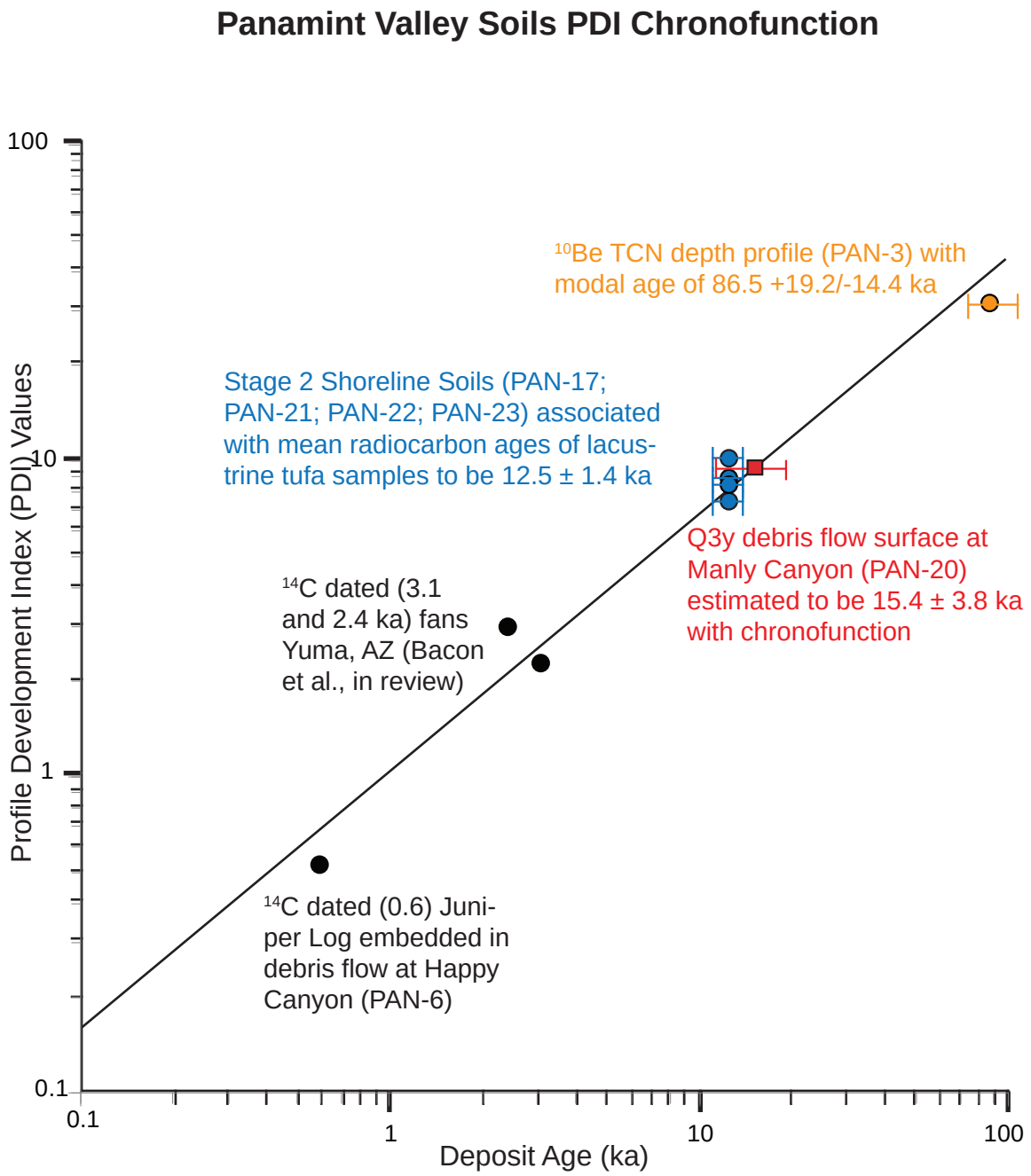

Figure 2-13: Profile Development Index (PDI) chronofunction of soils in Panamint Valley. Chronofunction can be inverted to provide soil age estimates based on calculated PDI values, as is the case of the Q3y surface (red square). All other soils plotted were used to calibrate the chronofunction. Black line represents the regression curve through these points, $r^2 = 0.97$. Uncertainties on radiocarbon ages (black circles) are within the size of the symbol.

developed on the 12.5 ± 1.4 ka shorelines range between 7.2 - 9.9 (Table 2.2), providing a sense of the range of variability. Although this variability probably increases with age, I feel this chronofunction provides a relatively robust chronology for soil development in Panamint Valley during the Holocene and Late Pleistocene.

2.7 Chronology of Alluvial Deposits

In addition to developing a chronofunction of soils in Panamint Valley to estimate the age of offset surfaces, I collected surface exposure samples from 8 boulders preserved atop the Q3y surface for ^{10}Be exposure dating at Manly Peak Canyon, and 4 terrestrial cosmogenic radionuclide depth profiles to constrain the age of the Q3o surface at Happy Canyon. Results from the depth profiles at Happy Canyon are pending, awaiting AMS analysis at PRIME Lab (Purdue).

2.7.1 Age of the Q3y Fan Surface at Manly Peak Canyon

Here I return to the question of the age of the Q3y surface at Manly Peak Canyon in an effort to determine slip rates along the Panamint Valley fault zone. The relationship between shoreline features and alluvial fans provides a refined age estimate for the Q3y surface. As noted above, MIS 2 shorelines (mean age of 12.5 ± 1.4 ka) are well-developed within the Q2 fan surface at Manly Peak Canyon (~86.5 +19.2/-14.4 ka) up to elevations of ~350 m. The lateral extent of these shorelines varies on the Q2 surface, and shorelines become progressively less well-developed around the apex of the fan to the south. Such shorelines are not present, however, at similar elevations across the lower

reaches Q3y surfaces (Figure 2-4). This relationship indicates that the Q3y surface postdates the formation of the low shorelines, an inference also made by previous workers (Smith, 1976; Zhang et al., 1990; Walker et al., 2005). Thus, I consider the mean age of the shorelines (dated at 12.5 ± 1.4 ka) as a maximum constraint on the age of the Q3y surface.

In order to compare soil development beneath the Q3y surface, I dug a pit just downslope of the debris-flow channel, on a smooth, unmodified part of the surface (Figure 2-14). Based on the Profile Development Index value for this pit, the soil chronofunction suggests an age of 15.4 ± 3.8 ka (Table 2.2; Figure 2-13)**.** Soil development at this site is quite similar to soils developed in the shorelines, an observation reinforced by similar PDI values of 9.4 for the Q3y surface and 8.3 - 9.9 for the beach ridge soil profiles. These PDI values are also consistent, within error, with cross-cutting relationships (e.g., Smith 1976; Zhang et al., 1990) suggesting that the Q3y surface is younger than the ~350 m shorelines. The similarity between PDI values from the Q3y surface and the beach ridge profiles suggests that the surfaces are close in age, and although the Q3y surface postdates shoreline formation (12.5 ± 1.4 ka), its PDI value suggests that it is not significantly younger. Therefore, based on the youngest age estimate from the chronofunction and the age of the shorelines, I assign a preferred age range for the Q3y surface of 11.6 – 13.9 ka.

As an additional test of this age, I collected samples from ten granitic boulders for exposure dating using in situ ^{10}Be (Gosse and Phillips, 2001). I selected boulders that were >1 m in diameter, and exhibited little evidence for weathering or spallation of the surface. All sampled boulders had minimal fractures, consistent coats of light-brown

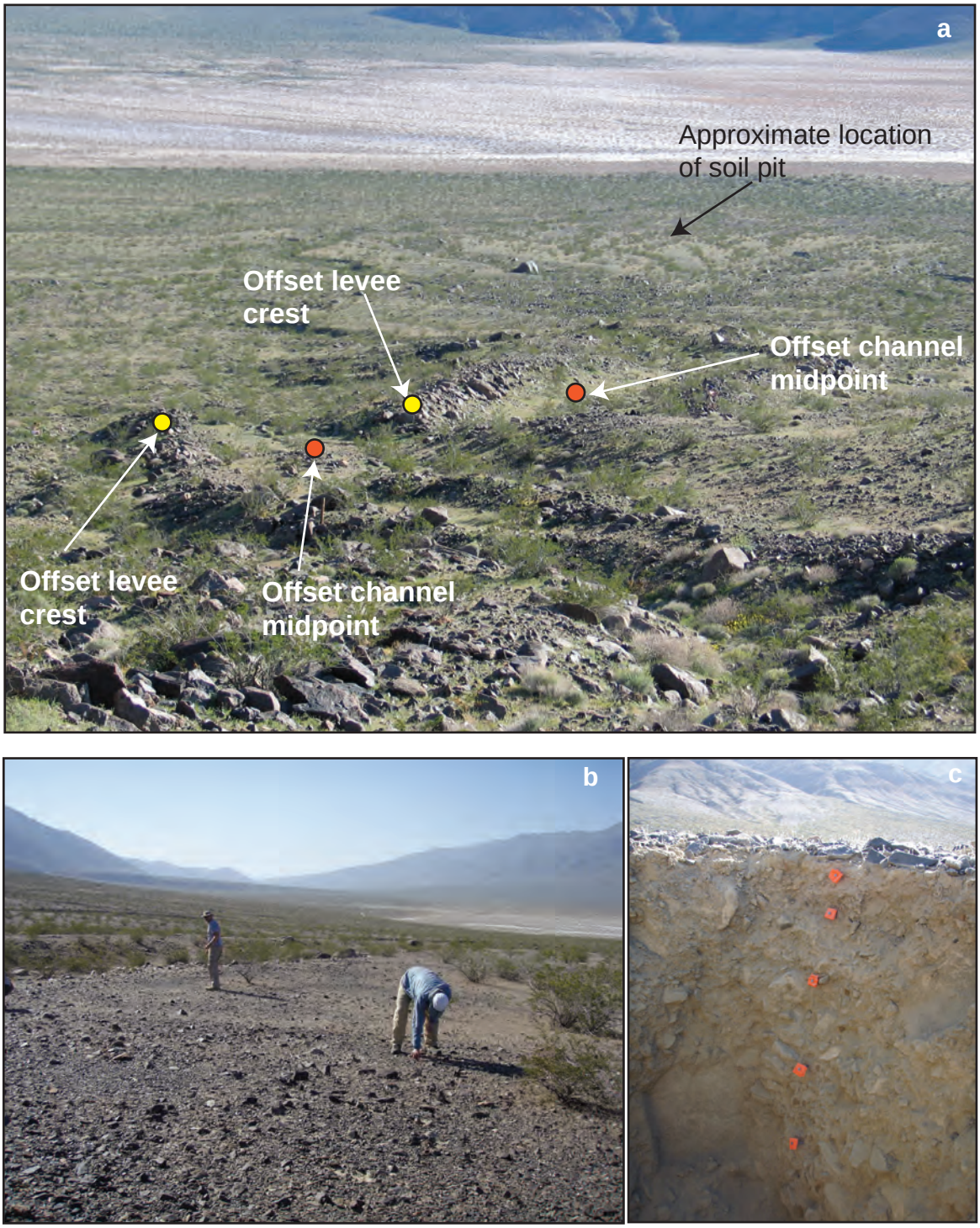

Figure 2-14: a) Down-fan view of offset debris flow levees on Q3y surface at Manly Peak Canyon with annotated offset features. b) Closer to the valley floor, the Q3y surface smooths into a moderately-developed desert pavement. Photo of location for soil pit PAN-20. c) Soil profile PAN-20 on Q3y surface. Soil description is in Table 2.2. PDI Value for PAN-20 is 9.4.

desert varnish, and smooth surfaces devoid of cm-scale relief between mineral constituents. Five of the samples were collected in close proximity to each other on the crest of the main offset debris flow levee and the other five samples were collected ~100 – 200 m down the same fan surface, where debris flow lobes are smoother, with well-developed pavements. I collected samples from the upper 1-3 cm of the boulder surface using a hammer and chisel, and I documented the average sample thickness for each boulder. The sample material was crushed and sieved to separate the 350-500 μm grain size fraction. Pure quartz was isolated by techniques outlined by Gosse and Phillips (2001). Samples were analyzed for ^{10}Be concentrations at PRIME Lab by accelerator mass spectrometry (AMS), and model exposure ages were determined using CRONUS-Earth online ^{10}Be exposure age calculator-version 2.2. Further details are available in Appendix C.

The interpretation of exposure ages may be complicated by factors such as the 1) extent of weathering and loss of boulder material from the boulder surface, 2) exhumation of previously buried boulders, and 3) inheritance of ^{10}Be acquired during erosion and transport of boulders (e.g., Gosse and Phillips, 2001). To minimize the influence of epistemic uncertainties associated with these processes, I sampled boulders that appear to have not rolled since deposition and show no history of post-depositional burial. Soil characteristics of the deposits showed no signs of significant erosion or degradation of the fan surface itself, and the lack of carbonate collars or varnish rings on the boulders above the ground surface corroborate this inference. Consequently, I consider exhumation of previously-buried boulders to be unlikely at this site. Similarly, the fresh, varnished, and unfractured surfaces of the boulders suggest minimal weathering

and loss of mass from the boulder surface. Therefore, I report the results from the CRONUS Earth online ^{10}Be exposure age calculator-version 2.2 using an erosion rate of 0 mm/ka (Table 2.4), a rate similarly used by Phillips et al. (1990). However, I acknowledge that any loss of mass from the boulder surface would lead to model ages that are somewhat older than those presented here.

^{10}Be surface exposure dates of eight boulder samples on the Manly Peak fan yield ages ranging from ~15–30 ka (Table 2.4). Using a probability density function to plot the distribution of age data, there is a single peak at ~20.1 ka (Figure 2-15). The arithmetic mean of the exposure ages is 21.6 ± 3.2 ka. A complete methods section including boulder sampling techniques, ^{10}Be model exposure age calculation, and analysis procedure is presented in Appendix C.

The rather large variance in boulder ages, combined with independent constraints on the age of the Q3y surface, suggest a significant component of inherited ^{10}Be within the boulders. Given that the youngest exposure age (15.2 ± 2.0 ka) is still older than the maximum allowable age of the Q3y surface inferred from the absence of MIS 2 shorelines, I conclude that inheritance is a significant part of the measured ^{10}Be concentrations. I note that if weathering and mass loss from the boulder surface were important at this site, the ages would be even older, and would further overestimate the true depositional age of the surface. Thus, these data provide a cautionary example of using boulder ages to estimate depositional ages of alluvial fans. In contrast to glaciated catchments, where inheritance may be minimized by vigorous glacial erosion (e.g., Bierman, 2007), one needs to account for this in fans with catchments dominated by fluvial and debris-flow erosion and transport.

Table 2.4. COSMOGENIC ^{10}BE ANALYSIS

Sample	Location (Latitude,Longitude)	Elevation (m)	Quartz[a] (g)	Average Thickness (cm)	Be Carrier[b] (g)	$^{10}Be/^{9}Be$, 10^{-12}	Measured ^{10}Be, 10^{5} atoms (g SiO_2)$^{-1}$	^{10}Be Exposure Age[c] (ka)
WH-PV-08-01	35°54.24, 117°11.12	438	39.94	1.00	0.3060	2.35 ± 0.08	4.72 ± 0.16	18.8 ± 2.4
WH-PV-08-02	35°54.13, 117°11.12	440	40.01	0.75	0.3083	2.65 ± 0.10	5.37 ± 0.21	21.3 ± 2.7
WH-PV-08-03	35°54.25, 117°11.10	443	40.00	2.75	0.3033	2.91 ± 0.06	5.79 ± 0.13	23.2 ± 2.9
WH-PV-08-06	35°54.26, 117°11.10	444	37.45	2.50	0.3102	1.76 ± 0.09	3.58 ± 0.18	15.2 ± 2.0
WH-PV-08-08	35°53.97, 117°11.22	386	40.00	2.00	0.3140	2.28 ± 0.09	4.71 ± 0.19	19.7 ± 2.5
WH-PV-08-09	35°53.82, 117°11.40	361	40.02	2.00	0.3050	3.08 ± 0.16	6.17 ± 0.32	26.2 ± 3.4
WH-PV-08-10	35°53.83, 117°11.40	361	40.06	1.50	0.3074	3.56 ± 0.35	7.18 ± 0.70	30.2 ± 4.9
WH-PV-08-12	35°53.88, 117°11.30	372	40.05	2.00	0.3865	1.73 ± 0.26	4.38 ± 0.66	18.5 ± 3.9

[a] A density of 2.6 g cm^{-3} was used for the granite surface samples

[b] Be carrier concentration is 995 μg mL^{-1}

[c] No erosion of surface boulders used

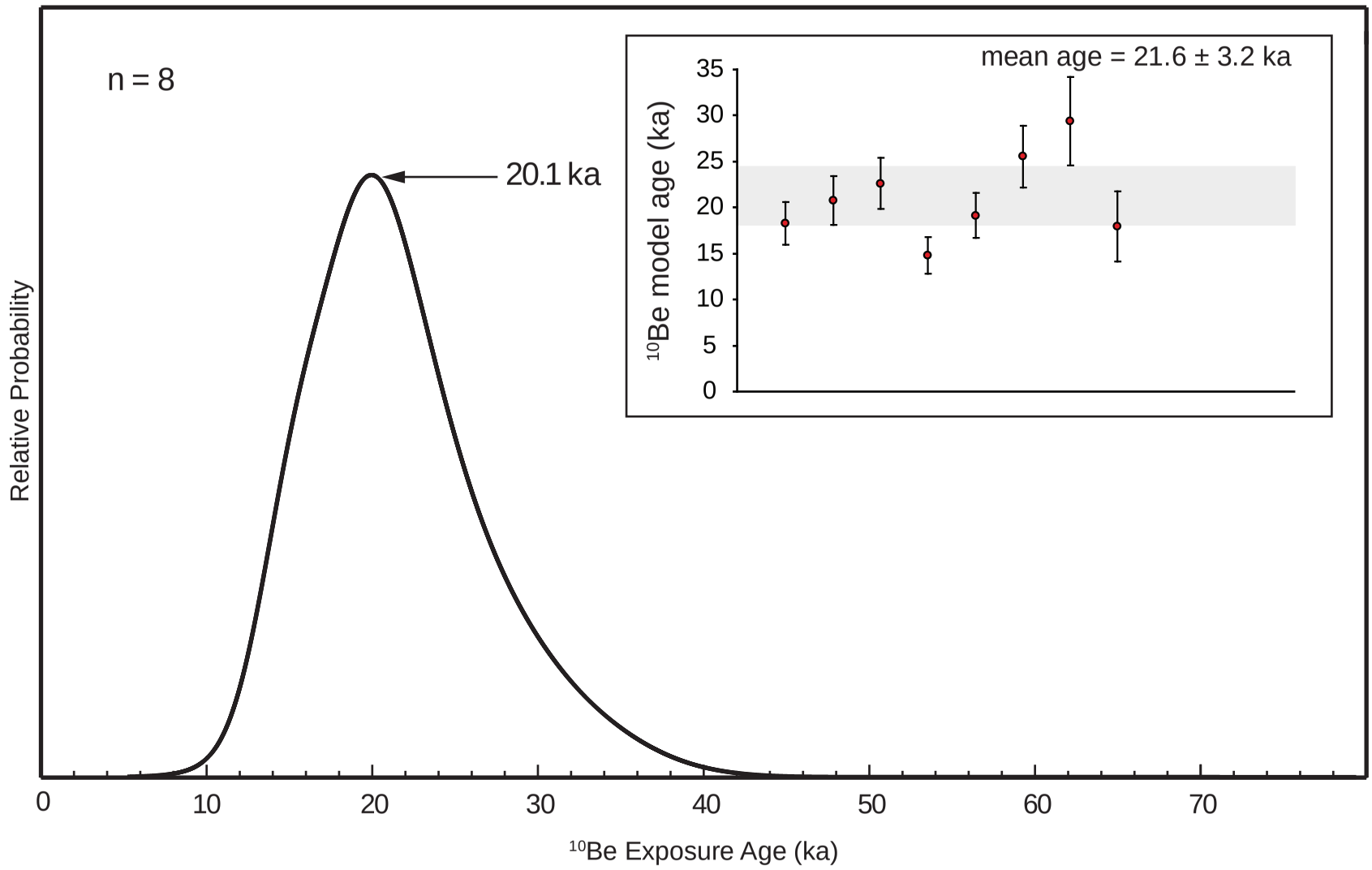

Figure 2-15: Probability density function (PDF) of the ^{10}Be ages from surface boulder samples on the offset Q3y debris flow surface at Manly Peak Canyon. The peak of the curve and mean of the exposure ages yield an age between 20-22 ka.

2.7.2 Age of the Q3o Fan Complex at Happy Canyon

Here I return to the question of the age of the Q3o surface at Happy Canyon in an effort to determine slip rates along the central PVFZ. As noted above, a network of distributed NE-trending dip-slip faults cut a fan surface I designate Q3o, broken into a lower Q3o complex and Q3o bench, both of which have moderate- to well-developed pavement, continuous varnish on clasts, and a moderate degree of soil development.

As noted above, a succession of wave-cut benches is present on the lower Q3o complex at Happy Canyon, with the highest of these shorelines at ~350 m. The lowest discernable shoreline is visible at 338 m elevation (Figure 2-10). Shorelines are not developed on any of the other alluvial fan deposits to the north and south at ~350 m elevation, suggesting that these surfaces post-date shoreline formation (12.5 ± 1.4 ka), and are Holocene in age. Most these alluvial deposits exhibit well-preserved surface morphology, incipient to light desert varnish, and poorly developed soils. Shoreline features are visible on the Q3o_a and Q3_b surfaces, with beach rock deposits, lacustrine tufa deposits, and shoreline construction features present. Airborne LiDAR images show more pronounced shoreline features on the Q3o_b surface than the Q3o_a surface, indicating that while both predate the Stage 2 lake, Q3o_b is slightly older than Q3o_a. Additionally, the youngest unit of the Q3o complex, Q3o_a, has been deposited on an abraded platform and has wave-cut features--suggesting that alluvial fan deposition and lake highstand occurred synchronously. This relationship provides a minimum age for the Q3o complex.

To establish a maximum age for the Q3o surface, I applied the PDI soil chronofunction to five soil profiles. Surface mapping and soil characterization from soil

profiles indicate that there are several generations of the lower Q3o complex (designated Q3o_a, Q3o_b, Q3o_c) that are part of the same fan complex and are nearly identical in surface morphology, but have varying degrees of soil development. The Q3o_a and Q3o_b surfaces inset the oldest Q3o_c unit (Figure 2-6), but all display a moderate to strong degree of clast varnish, moderate to well-developed desert pavements, and only traces of bar and swale morphology. PDI values for the lower Q3o alluvial fan complex range from 7.2 – 20.6, with associated chronofunction age estimates ranging from 11 – 40 ka. The PDI values for the Q3o_a inset range from 7.2 – 9.9 and range from 19.3 – 20.6 for the Q3o_b surface.

To constrain the age of the Q3o bench fan surface, I dug a soil pit on a smooth, unmodified part of the surface to better understand the relative age relationship between this surface and the lower Q3o complex. The PDI value on the Q3o bench is 11.9, within the range of PDI values on the low Q3o complex (7.2 – 20.6). Based on the PDI value for this pit, the soil chronofunction suggests an age of 20.7 ± 5.2 ka. Soil development at this site is quite similar to soils developed on the lower Q3o complex, consistent with the lower Q3o complex and Q3o bench being part of the same fan complex. By this assumption, displacement of the Q3o bench can be summed with displacement on the lower Q3o complex to evaluate the total amount of displacement on the Q3o surface.

As noted above, the relationship between the shoreline features and the Q3o_a alluvial fan provides a minimum age for the Q3o surface of 12.5 ± 1.4 ka. Although I know the minimum age of the Q3o complex to be 12.5 ± 1.4 ka, the Q3o_a surface is not heavily faulted, making it a non-ideal marker of displacement. Therefore, I use the soil chronofunction suggestion of 20.7 ± 5.2 ka for the age of Q3o bench as the minimum age

of the Q3o complex for slip rate calculations. To constrain the maximum age of the surface, I use age estimates derived from the Profile Development Index values of 6 soil profiles on the lower Q3o complex and Q3o bench, which yield corresponding age estimates between 11.0 and 40.4 ka. Based on the age estimates from the chronofunction of the Q3o bench and the lower Q3o complex, I assign a preferred age range for the Q3o surface of 20.7 – 40.4 ka. Additional age control on the Q3o surface will be provided from two ^{10}Be depth profiles: one on the Q3o bench, one on the lower Q3o_b surface. Samples are currently awaiting AMS measurement at PRIME Lab.

2.8 Fault Slip Rates

2.8.1 Slip Rate at Manly Peak Canyon

These results provide the first radiometric age control on displaced Pleistocene alluvial markers along the Panamint Valley fault zone. At Manly Peak Canyon, I calculate the horizontal projection of the slip vector by combining lateral offset of debris-flow levees with vertical displacement of the Q3y fan surface. This vector sum yields a total extension of 26.5 ± 3.8 m, in a direction toward ~325°. This estimate is similar to directions inferred by Walker and others (2005), but is a bit larger in magnitude as a result of the higher precision topographic data. I calculate a minimum slip rate based on the maximum surface age of 12.5 ± 1.4 ka, and a preferred maximum slip rate based on the lower limit ages allowed by the soil chronofunction (~11.6 ka). Given these bounds, the Late Pleistocene slip rate at Manly Peak Canyon is 2.1 ± 0.5 mm/yr in a direction toward ~325°. This rate is slightly greater than the rate determined by Zhang and others

(1990) for this same site (1.1 – 2.4 mm/yr), but is consistent with the Holocene slip rate of 2.4 ± 0.8 mm/yr inferred by Zhang et al. (1990) at Goler Wash, approximately 10 km south of the site used in this thesis.

2.8.2 Preliminary Slip Rates at Happy Canyon

At Happy Canyon, I calculate the horizontal displacement by summing the extension components of the offset Q3o surface. This yields a minimum total extension of 56.0 ± 10.3 m in a direction toward ~300˚. This displacement vector is the same as the one inferred by Walker et al. (2005). I calculate a minimum slip rate based on the maximum age estimated from the soil chronofunction of ~40 ka, and from the soil chronofunction age estimate on the Q3o bench of 20.7 ± 5.2 ka. Given these bounds, the minimum Late Pleistocene extension rate at Happy Canyon is broadly constrained to be 2.7 ± 1.5 mm/yr. Additionally, using the soil chronofunction age estimates of 20.7 ± 5.2 ka on the Q3o bench surface with a vertical offset of 68.1 ± 2.0 m produces a minimum throw rate of 3.3 ± 0.7 mm/yr along this portion of the PVFZ.

2.9 Discussion

2.9.1 Spatial Variations along the PVFZ

As previously noted, slip-rate estimates (extension and throw rates) from this thesis at Happy Canyon represent preliminary rates, which will be refined once results from four cosmogenic depth profiles are combined with chronofunction age estimates to

provide better constraints on the age of the offset Q3o surface. Therefore, assessments of how slip rates vary along the PVFZ remain tentative until I can compare two chronologically controlled slip-rate estimates along-strike of the PVFZ.

Using the map-view slip vectors, I can fully assess changes in displacement direction along-strike of the PVFZ from Manly Peak Canyon to Happy Canyon. Results from this thesis from slip-rate studies on two locations in Panamint Valley reveal changes along-strike from predominantly right lateral strike-slip faulting in southern Panamint Valley at Manly Peak Canyon to predominantly normal slip in central Panamint Valley at Happy Canyon. The map-view displacement vectors change from ~325° at Manly Peak Canyon to ~300° at Happy Canyon, with the extension direction along the PVFZ similar to the strike of the Hunter Mountain fault (trends N 50-60° W) in northern Panamint Valley (Figure 2-16).

The slip rates determined at Manly and Happy Canyon from summing the horizontal displacement components of faults at each site are similar, with the slip-rate estimate of 2.1 ± 0.5 mm/yr at Manly Canyon and 2.7 ± 1.5 mm/yr at Happy Canyon. However, the throw rate is much higher at Happy Canyon, which is found to be a minimum of 3.3 ± 0.7 mm/yr. This supports the idea by Walker and others (2005) that there is a greater amount of subsidence in northern Panamint Valley than in southern Panamint Valley, and that the transition occurs north of the intersection of the Manly Pass and Panamint Valley faults at Manly Peak Canyon.

In addition to changes in the horizontal displacement direction and throw rate along-strike of the PVFZ, results from this thesis suggest the possibility of slip-rate variations between southern and central – northern Panamint Valley. The slip-rate

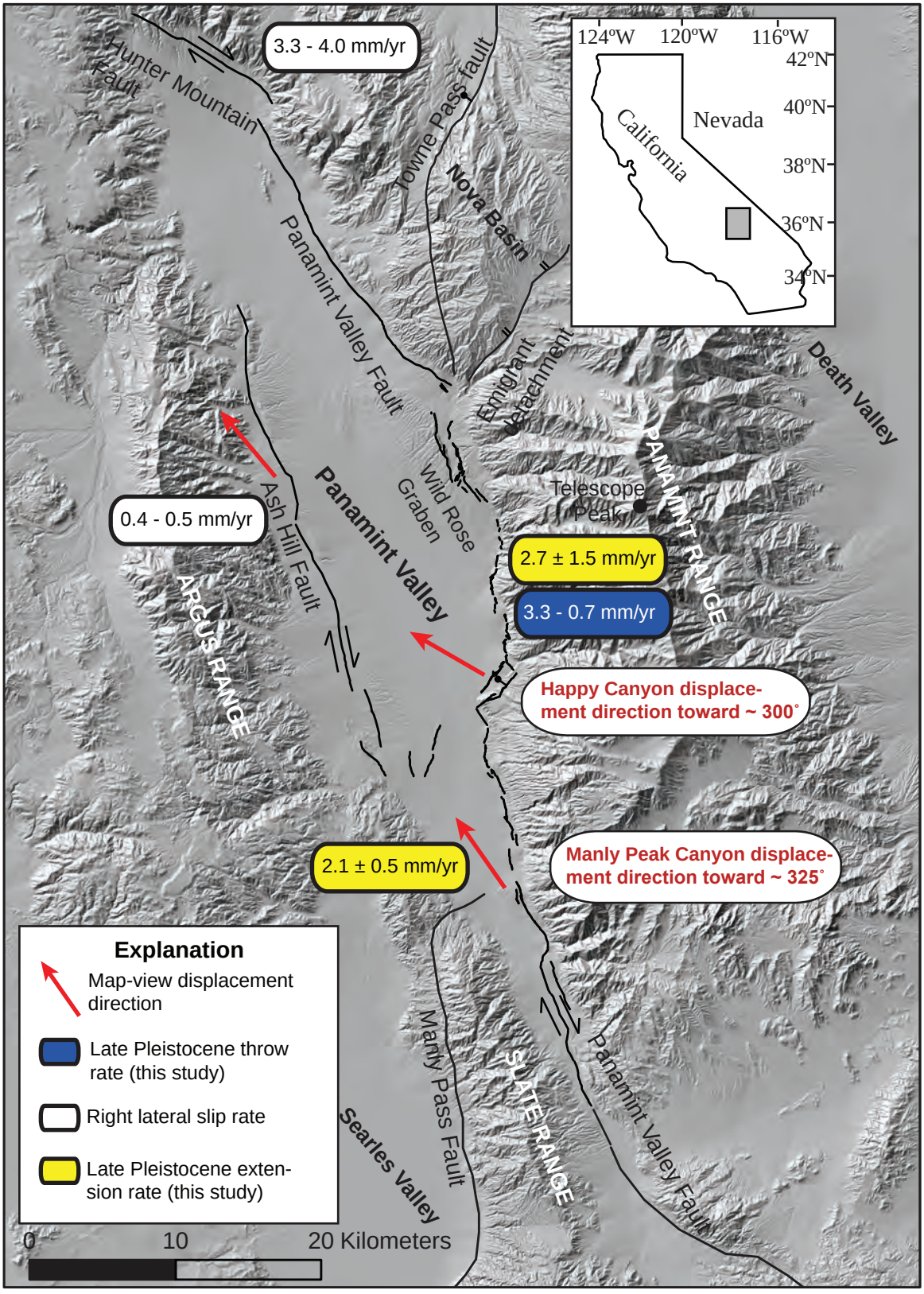

Figure 2-16: Summary of slip rates in Panamint Valley showing along-strike variations in displacement direction and throw rate along the PVFZ. Slip rate on the Hunter Mountain fault is from Oswald and Wesnousky (2002). Slip rate on the Ash Hill fault is from Densmore and Anderson (1997).

estimate of 2.1 ± 0.5 mm/yr at Manly Peak Canyon is well-constrained from cross-cutting relationships with dated shorelines and a minimum age constrained by soil characteristics and a calibrated soil chronofunction. The slip-rate estimate at Happy Canyon likely represents a minimum rate due to the projection uncertainties and initial fault dip assumptions when reconstructing fault slip. Therefore, even though the (extension) slip rates determined at Manly Peak and Happy Canyons in this study are similar, more refined age control at Happy Canyon may yield a slip-rate estimate closer in agreement with estimates along the Hunter Mountain fault of 3-4 mm/yr (e.g., Oswald and Wesnousky, 2002), supporting the idea that northern Panamint Valley is accommodating displacement at a faster rate than southern Panamint Valley.

Results from this study show that the PVFZ changes along-strike in throw rate from predominantly right lateral strike-slip faulting in the south, to a greater degree of normal-slip faulting in the north as it nears the right-lateral Hunter Mountain fault. How these variations are coordinated with slip variations on the Death Valley – Fish Lake Valley and Owens Valley – White Mountain fault systems, however, is still unclear. Based on slip-rate estimates from this thesis at two sites along the PVFZ compared with estimates along the Hunter Mountain fault, the PVFZ may experience a decrease in slip rate from 3-4 mm/yr (Hunter Mountain fault) to 2.1 ± 0.5 mm/yr (Manly Canyon in southern Panamint Valley), with similar slip-rate decreases from north to south on the aforementioned Death Valley – Fish Lake Valley and Owens Valley – White Mountain fault systems.

2.9.2 Tectonic Implications for the Eastern California Shear Zone

New slip-rate estimates along the PVFZ from this thesis can now be incorporated into creating a refined slip budget across the ECSZ at 36° N latitude. Summing geologic slip rates over Late Pleistocene time scales on the southern Owens Valley fault system (Sierra Nevada frontal fault, Little Lake/Airport Lake faults), southern Death Valley fault system (Black Mountain fault zone), and Panamint Valley fault zone show that the long-term geologic rates (~5-7 mm/yr) are still less than the short-term geodetic rates (9-12 mm/yr) across the ECSZ. Even with new slip-rate estimates from this thesis along the PVFZ, it remains difficult to reconcile geologic slip rates along structures north of the Garlock fault within the total rate of shear observed geodetically. This difficulty likely arises, in part, due to along-strike variations in displacement along faults, as seen with an increase in throw rate from south to north along the PVFZ. However, Late Pleistocene slip rates compared across the ECSZ at 36° N along the southern Owens Valley (<1 mm/yr Roquemore, 1988), Death Valley (<1-2 mm/yr, Klinger, 1999), and Panamint Valley fault zones (2.1 ± 0.5 mm/yr – 2.7 ± 1.5 mm/yr, this study) confirm that the PVFZ is the primary structure that accommodates right-lateral shear directly north of the Garlock fault.

Results from this study combined with previous rates determined along the Hunter Mountain fault zone of 3.3 – 4.0 mm/yr (Oswald and Wesnousky, 2002) suggest that slip rates on the Hunter Mountain – Panamint Valley fault zone also decrease southward closer to the Garlock fault, similar to spatial variations in slip rate observed on the Death Valley – Fish Lake Valley fault system and White Mountain – Owens Valley fault system. Slip gradients, such as the ones discussed above, are consistent with

relatively young faults that are still propagating at their southern tips. It remains unclear where deformation in the upper crust is located directly north of the Garlock fault. However, results from this thesis document the first slip rates with radiometric control along the southern Panamint Valley fault zone and, as such, provide key data with which to assess along-strike changes in slip on this major fault zone in the ECSZ.

References

Anderson, E.M. (1951), The dynamics of faulting, 2nd ed.: Edinburgh, Oliver and Boyd, 206 p.

Anderson, R. S., et al. (1996), Explicit treatment of inheritance in dating depositional surfaces using in situ ^{10}Be and ^{26}Al, *Geology*, *24*, 47-51.

Andrew, J., and J.D. Walker (2009), Reconstructing late Cenozoic deformation in central Panamint Valley, California; evolution of slip partitioning in the Walker Lane, *Geosphere*, *5*(3), 172-198.

Bacon, S. N., et al. (2006), Last glacial maximum and Holocene lake levels of Owens Lake, eastern California, USA, *Quaternary Science Reviews*, *25*(11-12), 1264-1282.

Bacon, S. N. and S.K. Pezzopane (2007), A 25,000-year record of earthquakes on the Owens Valley fault near Lone Pine, California: Implications for recurrence intervals, slip rates, and segmentation models, *Geological Society of America Bulletin*, *119*(7), 823-847.

Balco, G., et al. (2008), A complete and easily accessible means of calculating surface exposure ages or erosion rates from ^{10}Be and ^{26}Al measurements, *Quarternary Geochronology*, *3,* 174-195.

Bacon, S. N., et al. (In review), Timing and distribution of alluvial fan sedimentation in response to strengthening of late Holocene ENSO variability in the Sonoran Desert, southwesterm Arizona, Quaternary Research.

Bennett, R. A.., et al. (2003), Contemporary strain rates in the northern Basin and Range Province from GPS data, *Tectonics*, *22*(2), 1008.

Bierman, P. R. (1994), Using in situ produced cosmogenic isotopes to estimate rates of landscape evolution: A review from the geomorphic perspective, *Journal of Geophysical Research*, *99*, 13885-13896.

Bierman, P.R. (2007), Cosmogenic glacial dating, 20 years and counting, *Geology,35*(6), 575-576.

Birkeland, P.W. (1999), Soils and Geomorphology (3rd Ed.), New York, Oxford Univ. Press, 372 p.

Bischoff, J. L., et al. (1993), AMS radiocarbon dates on sediments from Owens Lake drill hole OL - 92, US Geological Survey, Report: Open File Report 93-0683, 246-250.

Burchfiel, B. C., and J. H. Stewart (1966), 'Pull-apart' origin of the central segment of Death Valley, California, *Geological Society of America bulletin*, *77*(4), 439-441.

Burchfiel, B. C., et al. (1987), Geology of Panamint Valley-Saline Valley pull-apart system, California; palinspastic evidence for low-angle geometry of a Neogene range-bounding fault, *Journal of Geophysical Research*, *92*(b10), 10422.

Cichanski, M. (2000), Low-angle, range-flank faults in the Panamint, Inyo, and Slate ranges, California; implications for recent tectonics of the Death Valley region, *Geological Society of America bulletin*, *112*(6), 871-883.

Cowgill, E., (2007), Impact of riser reconstructions on estimation of secular variation in rates of strike-slip faulting: Revisiting the Cherchen River site along the Altyn Tagh Fault, NW China, *Earth and Planetary Science Letters*, *254*(3-4), 239-255.

Cowie, P. A., and C. H. Scholz (1992), Displacement-length scaling relationship for faults: data synthesis and discussion, *Journal of Structural Geology*, *14*(10), 1149-1156.

Davis, G., and B. C. Burchfiel (1973), Garlock Fault: An Intracontinental Transform Structure, Southern California, *Geological Society of America bulletin*, *84*(4), 1407-1422.

Densmore, A. L., and R. S. Anderson (1997), Tectonic geomorphology of the Ash Hill Fault, Panamint Valley, California, *Basin research*, *9*(1), 53-63.

Desilets, D., et al. (2003), Spatial and temporal distribution of secondary cosmic-ray nucleon intensities and applications to in situ cosmogenic dating, *Earth and Planetary Science Letters*, *206*(1-2), 21-42.

Desilets, D., et al. (2006), Extended scaling factors for in situ cosmogenic nuclides; new measurements at low latitude, *Earth and Planetary Science Letters*, *246*(3-4), 265-276.

Dixon, T. H., et al. (2000), Present-day motion of the Sierra Nevada block and some tectonic implications for the Basin and Range Province, North American Cordillera, *Tectonics*, *19*(1), 1-24.

Dixon, T. H., et al. (2003), Paleoseismology and Global Positioning System: earthquake-cycle effects and geodetic versus geologic fault slip rates in the Eastern California shear zone, *Geology*, *31*(1), 55-58.

Dokka, R. K., and C. J. Travis (1990a), Late Cenozoic strike-slip faulting in the Mojave Desert, California, *Tectonics*, *9*(2), 311-340.

Dokka, R. K., and C. J. Travis (1990b), Role of the Eastern California Shear Zone in accommodating Pacific-North America plate motion, *Geophysical Research Letters*, *17*(9), 1323-1326.

Dolan, J.,et al. (2007), Long-range and long-term fault interactions in Southern California, *Geology*, *35*(9), 855-858.

Dunai, T. (2001), Influence of secular variation of the geomagnetic field on production rates of in situ produced cosmogenic nuclides, *Earth and Planetary Science Letters*, *193*(1-2), 197-212.

Faulds, J. E., et al. (2005), Kinematics of the northern Walker Lane: An incipient transform fault along the Pacific-North American plate boundary, *Geology*, *33*(6), 505-508.

Fialko, Y., et al. (2005), Three-dimensional deformation caused by the Bam, Iran, earthquake and the origin of shallow slip deficit, *Nature*, *435*(7040), 295-299.

Frankel, K., et al. (2007), Spatial variations in slip rate along the Death Valley-Fish Lake Valley fault system determined from LiDAR topographic data and cosmogenic (super 10) Be geochronology, *Geophysical Research Letters*, *34*(18), L18303.

Frankel, K., et al. (2007), Cosmogenic ^{10}Be and ^{36}Cl geochronology of offset alluvial fans along the northern Death Valley fault zone: implications for transient strain in the eastern California shear zone, *Journal of Geophysical Research*, *112*(b6), B06407.

Frankel, K., et al. (2008), Active tectonics of the Eastern California shear zone GSA Field Guide 11 Field Guide to Plutons Volcanoes Faults Reefs Dinosaurs and Possible Glaciation in Selected Areas of Arizona California and Nevada, *GSA Field Guide*, *11*, 43-81.

Friedrich, A., et al. (2003), Comparison of geodetic and geologic data from the Wasatch region, Utah, and implications for the spectral character of Earth deformation at periods of 10 to 10 million years, *Journal of Geophysical Research*, *108*(b4), 2199.

Gale, H.S. (1914), Salines in the Owens, Searles, and Panamint basins, southeastern California, *US Geological Survey Bulletin, 580,* 281-323.

Gan, W., et al. (2000), Strain accumulation across the eastern California shear zone at latitude 36 degrees 30'N, *Journal of Geophysical Research*, *105*(b7), 16229-16216.

Gan, W., et al. (2003), Initiation of deformation of the eastern California shear zone: constraints from Garlock Fault geometry and GPS observations, *Geophysical Research Letters*, *30*(10), 1496.

Gee, G.W., and D. Or (2002), Particle-size analysis; *In* Dane, J.H. and G.C. Topp (eds.), Methods of soil analysis, Part 4. Physical Methods, Soil Science Society of America Book Series 5, 255-293.

Gosse, J. C., and F. M. Phillips (2001), Terrestrial in-situ cosmogenic nuclides: Theory and application, *Quaternary Science Reviews*, *20*, 1475-1560.

Hancock, G., et al. (1999), Dating fluvial terraces with (super 10) Be and (super 26) Al profiles; application to the Wind River, Wyoming, *Geomorphology*, *27*(1-2), 41-60.

Harden, J. (1982), A quantitative index of soil development from field descriptions; examples from a chronosequence in central California, *Geoderma*, *28*(1), 1-28.

Heisinger, B., et al. (2002a), Production of selected cosmogenic radionuclides by muons; 1, Fast muons, *Earth and Planetary Science Letters*, *200*(3-4), 345-355.

Heisinger, B., et al. (2002b), Production of selected cosmogenic radionuclides by muons; 2, Capture of negative muons, *Earth and Planetary Science Letters*, *200*(3-4), 357-369.

Hidy, A., et al. (In review), A constrained Monte Carlo approach to modeling exposure ages from profiles of terrestrial cosmogenic nuclides: an example from Lees Ferry, AZ.

Hodges, K. V., et al. (1989), Evolution of extensional basins and Basin and Range topography west of Death Valley, California, *Tectonics*, *8*(3), 453-467.

Jannik, N. O., et al. (1991), A 36Cl chronology of lacustrine sedimentation in the Pleistocene Owens River system, *Geological Society of America bulletin*, *103*, 1146-1159.

Jayko, A. S., et al. (2008), Late Pleistocene lakes and wetlands, Panamint Valley, Inyo County, California Special Paper 439 Late Cenozoic Drainage History of the Southwestern Great Basin and Lower Colorado River Region Geologic and Biotic Perspectives, *Special papers*, *439*, 151-184.

Kirby, E. (2004), Late Quaternary-Recent slip on a low-angle normal fault; inferences from alluvial deposits along the Panamint Valley fault system, *Abstracts with Programs - Geological Society of America*, *36*(5), 547.

Kirby, E., et al. (2006), Temporal variations in slip rate of the White Mountain fault zone, eastern California, *Earth and Planetary Science Letters*, *248*(1-2), 153-185.

Kirby, E., et al. (2008), Late Pleistocene slip rate along the Owens Valley fault, eastern California, *Geophysical Research Letters*, *35*(1), L01304.

Klinger, R. E. (1999), Tectonic geomorphology along the Death Valley fault system - Evidence for recurrent Late Quaternary activity in Death Valley National Park, in *Proceedings of Conference on Status of Geologic Research and Mapping, Death Valley National Park*, edited by J. L. Slate, pp. 132-140, U.S. Geological Survey, Denver.

Knott, J.R. (2001), Field trip guide for Day C, central Death Valley: Stop C2, Late Pleistocene slip rate of the Black Mountains fault zone, U.S. Geological Survey Open-File Report: OF 01-0051, C92-C102.

Lal, D. (1991), Cosmic ray labeling of erosion surfaces; in situ nuclide production rates and erosion models, *Earth and Planetary Science Letters*, *104*(2-4), 424-439.

Le, K., et al. (2007), Late Quaternary slip rates along the Sierra Nevada frontal fault zone, California: Slip partitioning across the western margin of the Eastern California Shear Zone-Basin and Range Province, *Geological Society of America bulletin*, *119*(1), 240-256.

Lee, J., et al. (2001a), Quaternary faulting history along the Deep Springs fault, California, *Geological Society of America bulletin*, *113*(7), 855-869.

Lee, J., et al. (2001b), Holocene slip rates along the Owens Valley fault, California: Implications for the recent evolution of the Eastern California Shear Zone, *Geology*, *29*(9), 819-822.

Lee, J., et al. (2009), Exhumation of the Inyo Mountains, California; implications for the timing of extension along the western boundary of the Basin and Range Province and

distribution of dextral fault slip rates across the Eastern California shear zone, *Tectonics*, *28*(1), TC1001.

Lifton, N. (2005), Addressing solar modulation and long-term uncertainties in scaling secondary cosmic rays for in situ cosmogenic nuclide applications, *Earth and Planetary Science Letters*, *239*(1-2), 140-161.

Lin, J., et al. (1998), A reassessment of U-Th and (super 14) C ages for late-glacial high-frequency hydrological events at Searles Lake, California, *Quaternary Research*, *49*(1), 11-23.

McGill, S. (1991), Surficial offsets on the central and eastern Garlock Fault associated with prehistoric earthquakes, *Journal of Geophysical Research*, *96*(b13), 21597-21521.

McGill, S., and K. Sieh (1993), Holocene slip rate of the central Garlock fault in southeastern Searles Valley, California, *Journal of Geophysical Research*, *98*, 14,217-214,231.

McGill, S., et al. (2009), Slip rate of the western Garlock Fault, at Clark Wash, near Lone Tree Canyon, Mojave Desert, California, *Geological Society of America Bulletin*, 1-554.

Miller, M., et al. (2001), Refined kinematics of the Eastern California shear zone from GPS observations, 1993-1998, *Journal of Geophysical Research*, *106*, 2245-2263.

MIT, F. G. C., and S. Biehler (1987), A geophysical investigation of northern Panamint Valley, Inyo County, California, *Journal of Geophysical Research*, *92*, 10,427-410,441.

Monastero, F. C., et al. (1997), Evidence for post-early Miocene initiation of movement on the Garlock Fault from offset of the Cudahy Camp Formation, east-central California, *Geology*, *25*(3), 247-250.

Monastero, F. C., et al. (2002), Neogene Evolution of the Indian Wells Valley, east-central California, in *Geologic Evolution of the Mojave Desert and Southwestern Basin and Range*, edited by A. F. Glazner, et al., pp. 199-228, Geological Society of America Memoir 195.

Numelin, T., et al. (2007), Late Pleistocene slip on a low-angle normal fault, Searles Valley, California, *Geosphere*, *3*(3), 163-176.

Oskin, M., et al. (2007), Slip rate of the Calico Fault: implications for geologic versus geodetic rate discrepancy in the Eastern California shear zone, *Journal of Geophysical Research*, *112*(b3), B03402.

Oskin, M., et al. (2008), Elevated shear zone loading rate during an earthquake cluster in eastern California, *Geology*, *36*(6), 507-510.

Oswald, J., and S. G. Wesnousky (2002), Neotectonics and Quaternary geology of the Hunter Mountain fault zone and Saline Valley region, southeastern California, *Geomorphology*, *42*(3-4), 255-278.

Peltzer, G., et al. (2001), Transient strain accumulation and fault interaction in the Eastern California shear zone, *Geology*, *29*(11), 975-978.

Phillips, F. M., et al. (1990), Cosmogenic Chlorine-36 Chronology for Glacial Deposits at Bloody Canyon, Eastern Sierra Nevada, *Science*, *248*, 1529-1532.

Reheis, M. (1995), Quaternary soils and dust deposition in southern Nevada and California, *Geological Society of America Bulletin*, *107*(9), 1003-1022.

Reheis, M. (1996), Kinematics of the eastern California shear zone; evidence for slip transfer from Owens and Saline Valley fault zones to Fish Lake Valley fault zone, *Geology*, *24*(4), 339-342.

Reheis, M. C., and T. L. Sawyer (1997), Late Cenozoic history and slip rates of the Fish Lake Valley, Emigrant Peak, and Deep Springs fault zone, Nevada and California, *Geological Society of America bulletin*, *109*(3), 280-299.

Reimer, P. (2004), IntCal04 terrestrial radiocarbon age calibration, 0-26 cal kyr BP, *Radiocarbon*, *46*(3), 1029-1058.

Repka, J., et al. (1997), Cosmogenic dating of fluvial terraces, Fremont River, Utah, *Earth and Planetary Science Letters*, *152*(1-4), 59-73.

Rockwell, T. K., et al. (2000), Paleoseismology of the Johnson Valley, Kickapoo, and Homestead Valley faults: Clustering of earthquakes in the Eastern California Shear Zone, *Bulletin of the Seismological Society of America*, *90*(5), 1200-1236.

Roquemore, G. R. (1988), Revised estimates of slip-rate on the Little Lake fault, California, *Geological Society of America Abstracts with Programs*, *20*(3), 225.

Sauber, J., et al. (1994), Geodetic slip rate for the eastern California shear zone and the recurrence time of Mojave desert earthquakes, *Nature*, *367*, 264-266.

Schermer, E. R., et al. (1996), Late Cenozoic structure and tectonics of the northern Mojave Desert, *Tectonics*, *15*(5), 905-932.

Slate, J. L. (1992), Quaternary stratigraphy, geomorphology, and geochronology of alluvial fans, Fish Lake Valley, Nevada-California, Ph.D. thesis, 241 pp, University of Colorado, Boulder.

Slate, J. L. (Ed.) (1999), *Proceedings of Conference on Status of Geologic Research and Mapping, Death Valley National Park*, U.S. Geological Survey, Denver.

Smith, G. (1962), Large lateral displacement on Garlock fault, California, as measured from offset dike swarm, *Bulletin of the American Association of Petroleum Geologists*, *46*(1), 85-104.

Smith, G.I. and K.B. Ketner (1970), Lateral displacement on the Garlock Fault, southeastern California, suggested by offset sections of similar metasedimentary rocks, in *U.S. Geological Survey Professional Paper*, Report: P 0700-D, D1-D9.

Smith, G. (1983), *Pluvial lakes of the Western United States Late-Quaternary Environments of the United States*, 190 pp.

Smith, G. I., et al. (1983), Core KM-3, a surface-to-bedrock record of Late Cenozoic sedimentation in Searles Valley, California, in *Geological Survey Professional Paper*, edited, p. 24.

Smith, R. S. U. (1976), Late Quaternary pluvial and tectonic history of Panamint Valley, Inyo and San Bernardino counties, California, PhD thesis, 295 pp, Cal. Inst. of Tech., Pasadena.

Snyder, N. P., and K. V. Hodges (2000), Depositional and tectonic evolution of a supradetachment basin; (super 40) Ar/ (super 39) Ar geochronology of the Nova Formation, Panamint Range, California, *Basin research*, *12*(1), 19-30.

Staff, S. S. (1993), Examination and description of soils, *Soil Survey Manual USDA Handbook No. 18*, Soil Conservation Service, Chapter 3, US Government Printing Office, Washington, DC.

Stone, J. (2000), Air pressure and cosmogenic isotope production, *Journal of Geophysical Research*, *105*(b10), 23753-23723.

Stuiver, M. (1993), Extended (super 14) C data base and revised CALIB 3.0 (super 14) C age calibration program, *Radiocarbon*, *35*(1), 215-230.

Taylor, E. M. (1988), Instructions for the soil development index template-Lotus 1-2-3, *U.S. Geological Survey Open-File report*, *233A*.

Thompson, S., et al. (2002), Late Quaternary slip rates across the central Tien Shan, Kyrgyzstan, Central Asia, *Journal of Geophysical Research*, *107*(b9), 2203.

Walker, J., et al. (2005), Strain transfer and partitioning between the Panamint Valley, Searles Valley, and Ash Hill fault zones, California, *Geosphere*, *1*(3), 111-118.

Wells, S., et al. (1986), *Paleo-sheetflood bed forms on late Quaternary alluvial-fan surfaces in the Southwestern U.S.A Sediments down-under; 12th international sedimentological congress; abstracts*.

Wesnousky, S. G., and C. H. Jones (1994), Oblique slip, slip partitioning, spatial and temporal changes in the regional stress field, and the relative strength of active faults in the Basin and Range, western United States, *Geology*, *22*, 1031-1034.

Zhang, P., et al. (1990), Right-lateral displacements and the Holocene slip rate associated with prehistoric earthquakes along the southern Panamint Valley fault zone; implications for southern Basin and Range tectonics and coastal California deformation, *Journal of Geophysical Research*, *95*(b4), 4857-4872.

Appendix A: Reconstructing Slip on Faults

Strike Slip Faults

Using a topographic map of the site constructed from walking a detailed dGPS survey along the offset levees, a laser range finder, and airborne LiDAR data, I combine detailed field observations with high resolution images to map the trace of the fault and the best-preserved displaced levee features. Although the offset debris flow levees at Manly Canyon have been documented by previous workers (e.g., Smith, 1976; Zhang et al., 1990; Walker et al., 2005), no study, until now, has benefited from the acquisition of airborne laser swath mapping (ALSM; also known as LiDAR) digital topographic data along the PVFZ. The high resolution digital elevation data clearly show the offset debris flow levees, and provide an opportunity to precisely quantify the amount of displacement and restore the offset structures to their prefaulted position (e.g., Frankel et al., 2007a; Oskin et al., 2007).

I measured dextral offsets of debris flow levee crests, channel midpoints, and levee edges from the DEM, hill-shaded relief map, and a slope map. The fault obliquely cuts the channel, and due to erosion, several levee crests do not reach the mapped fault. Therefore, I projected the levee crests to the fault plane to determine the total amount of displacement of each offset feature. Despite the high precision associated with using LiDAR data, levee crest projection introduces a possible source of error. To account for this projection error, I determined the maximum and minimum offset for each piercing point by varying the projection by the width of the levee crests, or in the case of the channel midpoint, by the width of concave portion of the channel. I then calculated the

mean offset of the levees from four piercing points, and reported the mean and associated error as the amount of right lateral displacement of the Q3y surface.

Normal Faults

To reconstruct the dip-slip component of displacement along the PVFZ at the Happy Canyon and Manly Canyon slip-rate sites, I used topographic surveys from a combination of a differential GPS ground survey and airborne LiDAR digital elevation data across the normal faults at the mouth of Happy Canyon and Manly Canyon. Because these faults are dip-slip, I surveyed perpendicular to the fault strike, which I inferred to be parallel to the extension direction.

To reconstruct fault slip on an alluvial fan surface, I considered the case of a fault or multiple faults that cut an originally planar alluvial fan surface. I surveyed the present-day abandoned alluvial fan surfaces normal to the structural trend to reconstruct the vertical displacement across the normal fault. The survey represents points along the hanging wall surface slope, footwall surface slope, and across the fault that are then used to calculate hanging wall ($y_{hw} = m_{hw}x + b_{hw}$) and footwall ($y_{fw} = m_{fw}x + b_{fw}$) surfaces using least squares linear regression, where tangent of the alluvial fan dip, $\tan \alpha = m$ (Figure).

For the displacement reconstructions, I assume an initial fault dip angle (α) of 60° and project y_{hw} and y_{fw} to intersection points with the initial fault surface (x_{hw},y_{hw}; x_{fw}, y_{fw}), which is calculated using the midpoint of the present-day scarp face and a 60° slope. Total displacement (Dt), vertical displacement (Dv), and horizontal displacement (Dh)

are calculated for each fault, then are summed together to gain the total amount of vertical and horizontal displacement on the alluvial fan surface.

Several sources of error exist during the fault slip reconstruction calculations used in this thesis, as outlined above. To account for the uncertainties in fault slip calculations, I used Crystal Ball to run Monte Carlo simulations, which take into account the errors associated with initial fault angle and linear regressions of the hanging wall and footwall surfaces in the scarp profile. I considered uncertainties in initial fault dip to be $60 \pm 6°$, and uncertainties in slope (m) and intercept (b) based on least squares method for linear regression. The Monte Carlo simulation ran ten thousand calculations, with each trial simulation sampling a variety of probability distributions that represent uncertainty for each assigned variable. Because each parameter is characterized by a measurable mean and standard error, I used normal distributions to describe the probability density functions from the simulations. Frequency peaks define the probable fault slip displacements to 95% confidence levels (2σ), though in the final fault slip calculations I report 1 sigma error.

Appendix B: Radiocarbon ^{14}C Lacustrine Tufa Samples

I sampled in-situ, dense, nodose tufas at Happy Canyon and Manly Canyon near lacustrine beach gravels, abrasion platforms, and shoreline construction features, all suggesting that the samples are primary deposits from a shallow lake. Shoreline elevations were documented using a combination of LiDAR data and high-precision GPS measurements, and agree in all three locations within several meters.

Samples were sent to the NSF Arizona AMS Facility for preparation and analysis, where multiple acid leach steps for each sample were conducted. I report the ages from every leach step labeled A-C, with C representing the final leach step and the one I feel best represents the original age of the carbonate before atmospheric contamination (Table 1.3). Conventional ^{14}C dates reported in this study have been converted to calibrated ages using the CALIB v. 5.0.2 program (Stuiver and Reimer, 1993) with the INTCAL04 data set (Reimer et al., 2004) for all samples since the dates are younger than 20,000 yr BP.

Radiocarbon ^{14}C ages are categorized based on sample location, with three samples from Manly Canyon, five samples from what I termed lower Happy Canyon, taken ~20 m down-fan of the most prominent shoreline, and five samples from upper Happy Canyon, ~10 m down-fan of the shoreline. I averaged the calibrated ages exclusively from Happy Canyon and Manly Canyon, yielding an age of 12,500 ± 1,400 Cal yr BP.

I acknowledge that tufas in certain environmental conditions are susceptible to contamination with both older and younger carbon and can yield artificially inflated or deflated radiocarbon ages (e.g., Bischoff et al., 1993), and also may need to have

reservoir corrections applied to ^{14}C dates of tufas in lake systems (Benson, 1994; Lin et al., 2000). A reassessment of U-Th isochron and ^{14}C ages of lacustrine tufas in Searles Lake by Lin et al. (1998) showed that when ^{14}C ages were compared to U-series dates on the same tufa samples, reservoir-corrected ^{14}C dates yielded consistently younger ages, which they attributed to contamination of tufa outcrops from modern carbon. Therefore, I acknowledge the possibility that tufa ages yielded may underestimate the true age by ~ 1,000 yrs (Lin et al., 1998).

Appendix C: ^{10}Be Geochronology

^{10}Be Depth Profile on Manly Canyon Q2 Alluvial Fan

Cosmic rays continually bombard the Earth's surface, producing cosmogenic isotopes which interact with rock and soil, and accumulate in minerals that can be used to quantify the age of geomorphic features (e.g., Lal, 1991; Bierman, 1994; Gosse and Phillips, 2001). The total concentration of a cosmogenic radionuclide (CRN) in a sample from an alluvial deposit has two components: 1) the CRNs accumulated before deposition (inheritance) and 2) the CRNs accumulated following deposition. This concentration is a function of production rate, latitude, elevation, time of exposure, topographic shielding, and erosion rate. In alluvial fan surfaces, where inheritance can be large, the solution is to collect subsurface samples in a depth profile, so the inherited component can be separated from the in situ component (e.g., Anderson et al., 1996; Repka et al., 1997; Hancock et al., 1999; Kirby et al., 2006; Frankel et al., 2007a). For geomorphic applications, ^{10}Be is one the most commonly used cosmogenic isotopes, in large part because its main target mineral is quartz.

I collected a depth profile of five samples for ^{10}Be dating on the Q2 surface at Manly Canyon, with the deepest sample at ~1.5 m. Samples were prepared at University of Kansas using standard quartz separation methods from whole rock samples followed by successive etching to remove any remaining feldspar, meteoric components, and weathering products. Be was extracted from the pure quartz by anion and cation exchange chromatography. Samples were then sent and analyzed for ^{10}Be concentrations

by accelerator mass spectrometry (AMS) at Purdue Rare Isotope Measurement Laboratory (PRIME Lab).

Cosmogenic ^{10}Be samples exhibit an exponential decrease in concentration with depth. My interpretation of the age of the surface is based on a Monte Carlo ^{10}Be depth profile simulation model by Hidy et al. (in review), which allows site-specific geologic observations to be incorporated to better constrain exposure age, erosion rate, and inheritance. Data inputs include TCN concentration, TCN concentration error, sample depth, and sample thickness, and where available, cumulative bulk density above each sample. Model constraints for the Q2 surface assumes sample density to be between 1.9 and 2.1 g cm^{-3}. Total erosion for the model was assigned a range from 0 – 30 cm (0 – .5 cm/ka), based on soils and surface morphology, and erosion rate was considered constant and continuous with exposure time. Calculations use a ^{10}Be half-life of 1.387 Ma and use the revised value for ^{10}Be decay constant ($5.10 \pm 0.26 \times 10^{-7}$ yr^{-1}) and renormalization of reference ^{10}Be production rates (Balco, 2008). Production rate at the surface was assigned an uncertainty that includes the possible influence of minor surface uplift and factors in exposure and effects of the geomagnetic field, which are based on CRONUS-Earth online ^{10}Be exposure age calculator version 2.2 (Balco, 2008). Production by muons vs depth is based on a two-term exponential best fit for fast muons and a three-term exponential best fit for negative muon capture curves fit to the theoretical equations of Heisinger et al. (2002a, 2002b), down to a depth of 10 m.

The Monte Carlo simulation generates a depth profile and a reduced chi-squared value associated with that depth profile. It then determines if that chi-squared value is as good or better than the value generated from the data in the user's depth profile, given a

specified confidence window. The model continues this iterative process until a user-specified number of profiles pass the chi-squared test.

Surface age and uncertainty are reported along with best fits for inheritance and erosion rate on the Manly Canyon Q2 fan. At 2σ, 500,000 curves were fit to the ^{10}Be concentration data, yielding a minimum surface age of 72.1 ka, within 2σ uncertainty. The optimal exposure age produced by the model, based on the parameters yielding the best fit (lowest $\chi 2$ value), is 90.3 ka. However, I report the modal age value as the most appropriate exposure age, based on the highest frequency peak of all the profiles generated, which yields an age of 86.5 +19.2/-14.4 ka at 2σ. Additionally, I explored the effect of different erosion rates on the best fit age and found that for this site, the modal age is not very sensitive to changes in erosion rate.

^{10}Be Boulder Samples on Manly Canyon Q3y Debris Flow Surface

The criteria I used for boulder sampling was based on their shape, size, and degree of weathering. Selected boulders were chosen for having flat tops, heights of at least ~.5-1 meter off the ground, a strong degree of varnish suggesting little surface degradation, and minimal signs of fracture and spallation. Only boulders that appear to have not rolled since deposition and show no history of post-depositional burial were chosen for sampling. I collected samples from the upper 1 – 3 cm of the boulder surface using a hammer and chisel, and I documented the average sample thickness for each boulder. The sample material was crushed and sieved to separate the 350-500 um grain size fraction. Pure quartz was isolated by techniques outlined by Gosse and Phillips (2001). Samples were analyzed for ^{10}Be concentrations at PRIME Lab by accelerator

mass spectrometry (AMS), and model exposure ages were determined using CRONUS-Earth online ^{10}Be exposure age calculator-version 2.2. Updates on CRONUS-Earth online ^{10}Be exposure age calculator from Balco (2008) include a revised value for ^{10}Be decay constant and renormalization of reference ^{10}Be production rates. A detailed explanation of the recent changes can be found at http://hess.ess.washington.edu/math/docs/al_be_v22/al_be_docs.html. Table 2.4 shows location, elevation, density used (2.7 g cm-1 was used for the granite surface), sample thickness, measured ^{10}Be concentration, and ^{10}Be model age. Shielding factors were calculated from CRONUS and corrections for edge effects and surface slope are negligible. The ages are reported as a mean taken from three time-varying production models: Desilets et al. (2003, 2006), Dunai (2001), and Lifton et al. (2005). Internal uncertainties are only reported from the constant production rate model using the Lal (1991)/ Stone (2000) scaling scheme for spallation, though exposure ages and external uncertainties are reported for each time-varying production model. Internal uncertainties for the time-varying production models were calculated by dividing the internal uncertainties by the exposure ages reported from the constant production rate model using the scaling scheme of spallation from Lal (1991)/Stone (2000), then multiplying the exposure ages of the time-varying production models by the previously determined ratio. External uncertainties are reported using the largest value from the three time-varying production rate models.

I considered geologic and geomorphic evidence when interpreting age estimates from boulders at Manly Canyon, as the interpretation of exposure ages may be complicated by several factors. These include the extent of weathering and loss of

boulder material from the boulder surface, exhumation of previously buried boulders, and the inheritance component associated with the boulders. At Manly Canyon, all of the boulders on the fan surface show a strong degree of varnish, minimal signs of fracture and spallation, and lack carbonate collars or varnish rings above the ground surface, indicating a stable surface with very little erosion. Therefore, I report the results from the CRONUS Earth online ^{10}Be exposure age calculator-version 2.2 using an erosion rate of 0 mm/ka, a rate similarly used by Phillips et al. (1990).